Wave-packet dynamics in energy space of a chaotic trimeric Bose-Hubbard system

Moritz Hiller,[1] Tsampikos Kottos,[2] and Theo Geisel[3]
[1]*Physikalisches Institut, Albert-Ludwigs-Universität, Hermann-Herder-Straße 3, D-79104 Freiburg, Germany*
[2]*Department of Physics, Wesleyan University, Middletown, Connecticut 06459, USA*
[3]*MPI for Dynamics and Self-Organization, Bunsenstraße 10, D-37073 Göttingen, Germany*
and Department of Physics, University of Göttingen, Friedrich-Hund-Platz 1, D-37077 Göttingen, Germany
(Received 11 August 2008; published 19 February 2009)

We study the energy redistribution of interacting bosons in a ring-shaped quantum trimer as the coupling strength between neighboring sites of the corresponding Bose-Hubbard Hamiltonian undergoes a sudden change δk. Our analysis is based on a threefold approach combining linear response theory calculations as well as semiclassical and random matrix theory considerations. The δk borders of applicability of each of these methods are identified by direct comparison with the exact quantum-mechanical results. We find that while the variance of the evolving quantum distribution shows a remarkable quantum-classical correspondence (QCC) for all δk values, other moments exhibit this QCC only in the nonperturbative δk regime.

DOI: 10.1103/PhysRevA.79.023621 PACS number(s): 03.75.Lm, 34.50.Ez, 05.30.Jp, 05.45.Mt

I. INTRODUCTION

Understanding the intricate behavior of bosonic many-body systems has been a major challenge for leading research groups over the last years. Without doubt, the theoretical interest was strongly enhanced by recent experimental achievements in handling (ultra)cold quantum gases: Namely, since the celebrated realization of atomic Bose-Einstein condensates (BECs) in periodic optical lattices (OLs) [1–4] and the creation of "atom chips" [5–8], we have versatile tools at hand which allow for an unprecedented degree of precision as far as manipulation and measurement of the atomic cloud is concerned. While this has led, on the one hand, to novel, concrete applications of quantum mechanics like, e.g., atom interferometers [9–11] and lasers [1,4,12–14], it also enabled us to investigate complex solid-state phenomena, such as the Mott-insulator to superfluid transition [15] or the Josephson effect [3].

Beside these advances, our understanding of bosonic many-body systems is still very limited once we consider an (external) driving: In the framework of BECs in OLs, this can be, e.g., a modulation of the potential height or a tilting of the lattice. Due to the time dependence of the driving parameter, the energy of the system is not a constant of motion. On the contrary, the system experiences transitions between energy levels and therefore absorbs energy. This irreversible loss of energy is known as dissipation [16–19]. The classical dissipation mechanism is by now well understood [16], while quantum dissipation still poses some challenges. In order to get a better insight into the problem, the main task is to build a theory for the time-evolving energy distribution. Apart from being of fundamental interest, such a theory will also shed a new light on recent experiments with BECs in amplitude-driven OLs [20,21]. It has been pointed out that the energy absorption rate measurements can be used to probe the many-body excitations of the system [22–26].

In the present work, we approach the problem of quantum dissipation by studying the quantum dynamics of interacting bosons on a ring-shaped lattice consisting of three sites (trimer). Specifically, we will analyze the system's response to a rectangular pulse of finite duration t that perturbs the coupling $k_0 \to k = k_0 + \delta k$ between adjacent sites. In the framework of OLs this corresponds to a sudden change in the intensity of the laser field and is readily achieved in the experiment [20,21]. The associated dynamical scenario known as *wave-packet dynamics* [18,27–29] is one of the most basic nontrivial evolution schemes. Its analysis will pave the way to understand more demanding evolution scenarios and ultimately the response of interacting bosons under persistent driving.

The minimal quantum model that describes interacting bosons on a lattice with M wells is the Bose-Hubbard Hamiltonian (BHH), which incorporates the competition between kinetic and interaction energy of the bosonic system. The BHH is based on an M-mode approximation and hence its validity is subject to the specific conditions discussed in Refs. [2,30–32] (see also Sec. II). As far as the BHH is concerned, the two-site system (dimer) has been analyzed thoroughly from both the classical (mean-field) [33–35] and the purely quantum viewpoints [33,36,37] and many exciting results were found including their experimental realization [38].

As a matter of fact, the dimer is integrable since the BHH has two conserved quantities: the energy and number of bosons. The addition of a further site—yielding either a linear chain (open boundary conditions) or a ring (periodic boundary conditions)—is sufficient to make the resulting system (trimer) nonintegrable and thus leads to (classically) chaotic behavior. Here we consider a three-site ring[1] which can be experimentally realized using optical lattice or microtrap technology [6–8,39]. For example, an optical potential in a ring configuration can be achieved by letting a plane wave interfere with the so-called Laguerre-Gauss laser modes as described in [40,41]. Another possibility to experimentally create a three-site ring BEC trap [87] is given by a combination of the methods described in Refs. [42,43]: In the experiment of [42] a trapping potential is partitioned into

[1]We expect qualitatively similar results for a linear chain configuration.

three sections by a central repulsive barrier created with blue-detuned laser light that is shaped to segment the harmonic oscillator potential well into three local potential minima. For better optical resolution (up to 1.2 μm) and control of the coupling between the three condensates, one can substitute the detuned laser source of Ref. [42] with the one used in [43].

The motivation to study the quantum trimer is twofold: That is, while remaining simple enough to allow for a thorough analytical study, it displays a whole new class of complex behaviors which are typical for longer lattices consisting of many sites. The trimer has been studied quite extensively in the classical (mean-field) regime [44–46]. Less attention was paid to the analysis of the quantum trimer [29,47–52]. As a matter of fact, the majority of these studies is focused on the statistical properties of levels [47,48,53], while recently an analysis of the shape of eigenstates was performed in Ref. [29]. However, knowledge of spectral and wave-function statistics is not enough if one wants to predict the dynamical behavior of a system.

In our study we combine three theoretical approaches: On the one hand, we will use linear response theory (LRT), which constitutes the leading framework for the analysis of driven systems [18]. On the other hand, we employ an improved random matrix theory (IRMT) modeling. Although random matrix theory (RMT) was proven to be a powerful tool in describing *stationary* properties (like level statistics [48,53] and eigenfunctions [29]), its applicability to the description of wave-packet dynamics is not obvious [19,28]. The latter involves not only knowledge of the statistical properties of the two quantities mentioned above, but also the specific correlations between them. Finally, we will investigate the validity of semiclassical methods to describe the quantum evolution. Our analysis indicates that some moments of the evolving energy distribution show a remarkable level of quantum-classical correspondence (QCC) [19,27,28], while others are strongly dominated by quantum interference phenomena.

The structure of this paper is as follows: in the next section, we introduce the Bose-Hubbard Hamiltonian that mathematically describes a quantum three-site ring lattice. We identify its classical limit, leading to the discrete nonlinear Schrödinger equation, and derive the classical equations of motion. In Sec. III we discuss the notion of wave-packet dynamics and introduce the observables studied in the rest of the paper. We begin our analysis with the statistical properties of the spectrum and of the matrix elements of the BHH (Sec. IV). This study allows us to introduce an IRMT modeling which is presented in Sec. IV D. In Sec. V we extend our previous analysis on the parametric evolution of the eigenstates of the BHH [29] by comparing the actual quantum-mechanical calculations with the results of the IRMT modeling. We introduce the concept of parametric regimes [29] and show how it can be applied to analyze the parametric evolution of the local density of states (LDOS) [19,29,54]. We then turn to the dynamics of the BHH (Sec. VI) and extend the notion of regimes to the wave-packet dynamics scenario. The predictions of LRT, IRMT modeling, and semiclassics are compared with the exact quantum-mechanical calculations for the trimeric BHH model. We find that the energy spreading $\delta E(t)$ shows a remarkable quantum-classical correspondence which is independent of the perturbation strength δk. In contrast, other observables are sensitive to quantum interference phenomena and reveal QCC only in the semiclassical regime. The latter can be identified with the nonperturbative limit associated with perturbations $\delta k > \delta k_{\mathrm{prt}}$. Section VII summarizes our findings.

II. BOSE-HUBBARD HAMILTONIAN

The mathematical model that describes interacting bosons in a (three-site) lattice is the Bose-Hubbard Hamiltonian, which in second quantization reads

$$\hat{H} = \frac{U}{2}\sum_{i=1}^{3} \hat{n}_i(\hat{n}_i - 1) - k\sum_{i\neq j} \hat{b}_i^\dagger \hat{b}_j, \quad \hbar = 1. \tag{1}$$

Here we consider a three-site ring configuration which is experimentally feasible with current optical methods where, for example, the trapping potential is created by letting a plane-wave interfere with the so-called Laguerre-Gauss laser modes as described in [40]. The operators $\hat{n}_i = \hat{b}_i^\dagger \hat{b}_i$ count the number of bosons at site i. The annihilation and creation operators $\hat{b}_i$ and $\hat{b}_i^\dagger$ obey the canonical commutation relations $[\hat{b}_i, \hat{b}_j^\dagger] = \delta_{i,j}$. In the BEC framework, $k = k_0 + \delta k$ is the coupling strength between adjacent sites i and j, and can be controlled experimentally (in the context of optical lattices this can be achieved by adjusting the intensity of the laser beams that create the trimeric lattice), while $U = 4\pi\hbar^2 a_s / m V_{\mathrm{eff}}$ describes the interaction between two atoms on a single site (m is the atomic mass, a_s is the s-wave scattering length of atoms which can be either positive or negative, and V_{eff} is the effective mode volume). It is interesting to note that the BHH also appears in the context of molecular physics where [36,55] k represents the electromagnetic and mechanical coupling between bonds of adjacent molecules i and j, while U represents the anharmonic softening of the bonds under extension.

The Bose-Hubbard model for M sites is based on a M-mode approximation [30] [in the limit of long lattices this corresponds to a single- (lowest-) band approximation of the OL [2]]. This assumption holds provided that the chemical potential, the kinetic energy, and the interaction energy are too low to excite states in the higher single-well modes (higher Bloch bands accordingly). Therefore, the lattice must be very deep [30,31,56], inducing large band gaps. Furthermore, the interaction energy has to be smaller than the single-particle ground-state energy, so as to not considerably modify the single-particle wave function. A Gaussian approximation of the wave function together with a standard harmonic trap of size 10 μm and a scattering length $a_s = 5$ nm indicates that the BHH model is valid for up to several hundred bosons per trap [30].

Hamiltonian (1) has two constants of motion: namely, the energy E and the number of particles, $N = \Sigma_{i=1}^{3} n_i$. Having $N = \mathrm{const}$ implies a finite Hilbert space of dimension $\mathcal{N} = (N+2)(N+1)/2$ [36,47], which can be further reduced by taking into account the threefold permutation symmetry of the model [29].

For large particle numbers $N \gg 1$ one can adopt a semiclassical approach for Hamiltonian (1). Formally, this can be seen if we define rescaled creation and annihilation operators $\hat{c}_i = \hat{b}_i / \sqrt{N}$. The corresponding commutators $[\hat{c}_i, \hat{c}_j^\dagger] = \delta_{ij}/N$ vanish for $N \gg 1$, and therefore one can treat the rescaled operators as c numbers. Using the Heisenberg relations $\hat{c}_i \to \sqrt{I_i} e^{i\varphi_i}$ (φ_i is an angle and I_i is the associated action[2]), we obtain the classical Hamiltonian $\mathcal{H}$:

$$\tilde{\mathcal{H}} = \frac{\mathcal{H}}{N\tilde{U}} = \frac{1}{2}\sum_{i=1}^{3} I_i^2 - \lambda \sum_{i \neq j} \sqrt{I_i I_j} e^{i(\varphi_j - \varphi_i)}, \tag{2}$$

where $\tilde{U} = NU$ is the rescaled on-site interaction.

The dynamics is obtained from (2) using the canonical equations $dI_i/d\tilde{t} = -\partial\tilde{\mathcal{H}}/\partial\varphi_i$ and $d\varphi_i/d\tilde{t} = \partial\tilde{\mathcal{H}}/\partial I_i$. Here $\tilde{t} = \tilde{U}t$ is the rescaled time. The classical dynamics depends both on the scaled energy $\tilde{E} = E/\tilde{U}N$ and the dimensionless parameter $\lambda = k/\tilde{U}$ [35,45,47,49,57]. For $\lambda \to 0$ the interaction term dominates and the system behaves as a set of uncoupled sites (also known as the *local-mode* picture [36]), while in the opposite limit of $\lambda \to \infty$, the kinetic term is the dominant one (*normal-mode* picture [34,57,58]). In both limits the motion is integrable, while for intermediate values of λ the trimeric BHH (1) has a chaotic component [48]. We point out that the classical limit is approached by keeping λ and $\tilde{U}$ constant, while $N \to \infty$ [29]. This is crucial in order to keep the underlying classical motion unaffected.

III. PRELIMINARY CONSIDERATIONS AND OBJECT OF THE STUDY

In this paper we study the trimeric BHH model (1) as a control parameter, the coupling strength between lattice sites is changed—i.e., $k_0 \to k_0 + \delta k$. In our analysis, we therefore consider

$$\hat{H} = \hat{H}_0 - \delta k(t)\hat{B}, \tag{3}$$

where the perturbation operator $\hat{B}$ is

$$\hat{B} = \sum_{i \neq j} \hat{b}_i^\dagger \hat{b}_j \tag{4}$$

and the unperturbed Hamiltonian $\hat{H}_0$ is given by Eq. (1) with $k = k_0$. Quantum mechanically, we work in the $\hat{H}_0$ eigenbasis. In this basis $\hat{H}_0$ becomes diagonal—i.e., $\mathbf{E}_0 = E_m^{(0)} \delta_{mn}$, where $\{E_m^{(0)}\}$ are the ordered eigenvalues and we can write

$$\mathbf{H} = \mathbf{E}_0 - \delta k \mathbf{B}. \tag{5}$$

Throughout this work we *always* assume that the perturbed Hamiltonian $\mathcal{H}(k)$ and the unperturbed Hamiltonian $\mathcal{H}(k_0)$ generate classical dynamics of the *same nature*—i.e., that the perturbation $\delta k = k - k_0$ is *classically small*, $\delta k < \delta k_{\mathrm{cl}}$ (see beginning of the next section for the definition of δk_{cl}).

[2]The quantum-mechanical conservation of the particle number N translates into conservation of total action $I = \Sigma_i I_i$.

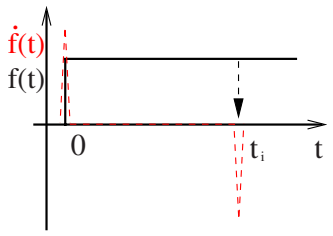

FIG. 1. (Color online) Scheme of the wave-packet dynamics scenario: the perturbation is a rectangular pulse of duration t_i at which the measurement is done. The function $f(t)$ represents the rescaled time dependence of the perturbation $\delta k(t) = \delta k\, f(t)$ (black line), while the dashed red line indicates its time derivative $\dot{f}(t)$.

This assures the applicability of classical LRT. Note, however, that this assumption is not sufficient to guarantee the validity of quantum-mechanical linear response theory. Our aim is to identify novel quantum-mechanical effects that influence the classical LRT results as the perturbation δk increases. At the same time, we address the implications of classically chaotic dynamics for the trimeric BHH and the route to quantum-classical correspondence in the framework of wave-packet dynamics.

For later purposes it is convenient to write the perturbation as $\delta k(t) = \delta k\, f(t)$ where δk controls the "strength of the perturbation," while $f(t)$ is the scaled time dependence [note that if we had $f(t) \propto t$—i.e., persistent driving—then δk would be the "rate" of the driving]. Although our focus will be on the wave-packet dynamics scenario where the perturbation is a rectangular pulse of strength δk and duration t—see Fig. 1 for a sketch of the resulting step function $f(t)$ with $k(t) = k(0)$—we expect that the results presented here will shed some light on the response of BHHs in the presence of more demanding driving scenarios.

A. Measures of the evolving distribution $P_t(n|n_0)$

In this subsection we discuss a number of observables that will allow us to quantify the response of the system and the spreading of the energy distribution.

We consider an initial microcanonical preparation described by an eigenstate $|n_0\rangle$ of the unperturbed Hamiltonian $\hat{H}(k(0))$. Given the driving scenario $k(t)$, it is most natural to analyze the evolution of the probability distribution

$$P_t(n|n_0) = |\langle n|\hat{U}(t)|n_0\rangle|^2, \tag{6}$$

where

$$\hat{U}(t) = \hat{T}\exp\left(-\frac{i}{\hbar}\int_0^t dt' \hat{H}(k(t'))\right) \tag{7}$$

is the time-ordered evolution operator and $\hat{H}(k(t))|n(k(t))\rangle = E_n(k(t))|n(k(t))\rangle$. By convention, we order the states by their energy. Hence we can regard $P_t(n|n_0)$ as a function of $r = n - n_0$ and average over the initial preparation (around some *classically* small energy window), so as to get a smooth distribution $P_t(r)$.

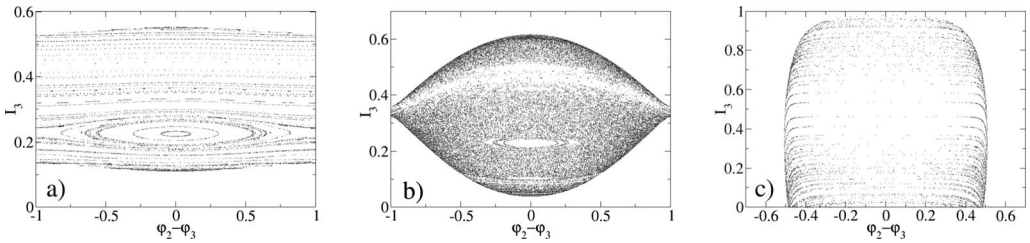

FIG. 2. Poincaré sections of the phase space belonging to the classical trimer for $N=1$ and different parameter values (a) $\lambda=0.005$, (b) $\lambda=0.05$, and (c) $\lambda=2$. On the y axis we plot the action I_3, while on the x axis the difference $\varphi_2-\varphi_3$ (in units of π) is plotted. The Poincaré section corresponds to the plane $\varphi_1=\varphi_3$ and $\dot{\varphi}_1>\dot{\varphi}_2$ of the energy surface $\tilde{E}=0.2$.

To capture various aspects of the evolving probability distribution $P_t(n|n_0)$, we introduce here the survival probability defined as

$$P(t)=|\langle n_0|\hat{U}(t)|n_0\rangle|^2=P_t(n_0|n_0) \tag{8}$$

and the energy spreading

$$\delta E(t)=\sqrt{\sum_n P_t(n|n_0)(E_n-E_{n_0})^2}, \tag{9}$$

which probes the tails of the evolving distribution. Yet the evolution of $P_t(n|n_0)$ is not completely captured by any of these measures: As we will see in Sec. VI, the wave functions can develop a "core" which is a result of a nonperturbative mixing of levels [29]. We therefore define an operative measure that reflects the creation of the "core," as the width δE_{core} which contains 50% of the probability:

$$\delta E_{\text{core}}(t)=[n_{75\%}-n_{25\%}]\Delta. \tag{10}$$

Here, Δ is the mean level spacing and n_q is determined through the equation $\Sigma_n P_t(n|n_0)=q$.

IV. STATISTICAL PROPERTIES OF THE TRIMERIC BHH: SPECTRA AND BAND PROFILE

The dynamical properties of the classical trimer were thoroughly investigated in a number of papers [44–46]. It was found that for intermediate values of the control parameter λ, the system exhibits (predominantly) chaotic dynamics. Some representative Poincaré sections [corresponding to the plane $\varphi_1=\varphi_3$ and $\dot{\varphi}_1>\dot{\varphi}_2$ of the energy surface $\tilde{E}=0.2$ of Hamiltonian (2)] of the phase space are reported in Fig. 2. As λ decreases, one can clearly see the transition from integrability to chaotic dynamics and back to integrability. We determine the regime of predominantly chaotic motion based on the nature of the phase space and the power spectrum $\tilde{C}(\tilde{\omega})$ of the classical perturbation operator (the latter is discussed in detail in Sec. IV B). While regular motion results in isolated peaks in $\tilde{C}(\tilde{\omega})$, a continuous (but possibly structured) power spectrum indicates chaoticity. Accordingly, the classical smallness condition $\delta k \ll \delta k_{\text{cl}}$ can be operatively defined as the perturbation strength that leaves $\tilde{C}(\tilde{\omega})$ unaffected. We have found that for $0.04<\lambda=k/\tilde{U}<0.2$ and an energy interval $\tilde{H}\approx 0.26\pm 0.02$ the motion is predominantly chaotic. Choosing our parameter values to be $k_0=15$ and $\tilde{U}=280$, we find $\delta k_{\text{cl}}\approx 20$.

In the following we will concentrate on the above-mentioned range of λ values for which chaotic dynamics is observed. The main question we will address is the following: What are the signatures of classical chaos in various statistical quantities upon quantization? As we shall see in the following subsections, chaos manifests itself mainly in two quantities: the spectral statistics of the eigenvalues $\{E_m^{(0)}\}$ and the averaged profile $\langle|\mathbf{B}_{mn}|^2\rangle$ of the perturbation operator. While the statistical properties of the levels have attracted some attention in the past [47,59], the traces of chaotic dynamics in the shape of the perturbation operator $\langle|\mathbf{B}_{mn}|^2\rangle$ and the statistical properties of its matrix elements were left unexplored. In the next subsections we will address these issues in detail and propose an improved random matrix theory modeling which takes our statistical findings into consideration.

A. Energy levels

In Fig. 3 we plot the parametric evolution of the eigenvalues $\tilde{E}_n^{(0)}$ as a function of λ for fixed effective interaction strength $\tilde{U}=280$. From Fig. 3 one observes that the spectrum becomes rather regular for very large λ. Indeed, for $\lambda\to\infty$ a

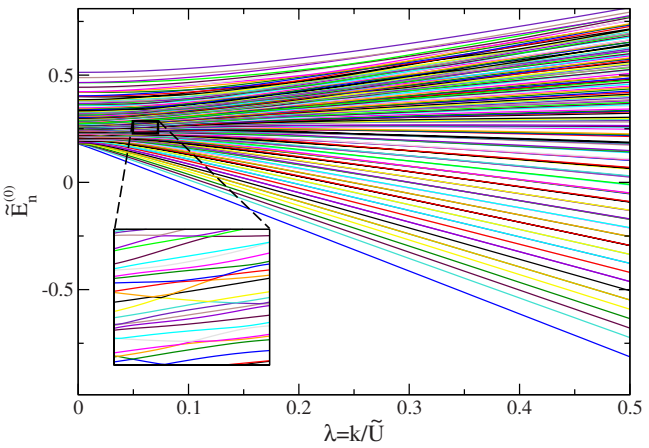

FIG. 3. (Color online) Parametric evolution of the eigenvalues $\tilde{E}_n^{(0)}$ as a function of the parameter λ. The number of bosons is $N=40$, and the effective interaction strength is $\tilde{U}=280$. In the main figure the entire spectrum is plotted, while the inset is a magnification of the small box. One observes a qualitative change in the spectrum as λ is changed. See text for details.

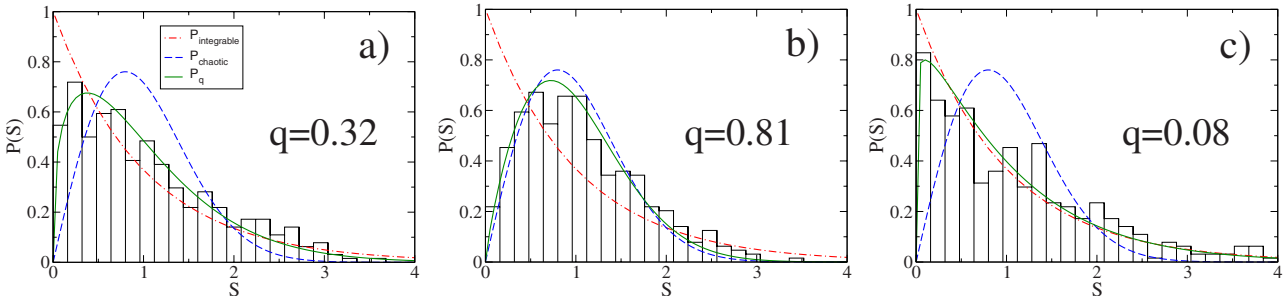

FIG. 4. (Color online) The level spacing distribution $\mathcal{P}(S)$ of the BHH trimer for three representative values of the dimensionless ratio $\lambda=k/\tilde{U}$, which controls the underlying classical dynamics: (a) $\lambda=0.025(k=7)$, (b) $\lambda=0.05(k=14.5)$, and (c) $\lambda=0.35(k=100)$. The red dash-dotted line corresponds to the Poissonian distribution (14), which is expected for integrable systems: the dashed blue line corresponds to the Wigner surmise (13) (chaotic systems), while the solid green line represents the fitted Brody distribution (15). In Fig. 15 we report the fitted Brody parameter q for various values of λ. The system corresponds to $N=230$ bosons and $\tilde{U}=280$. The histograms include the 400 relevant levels around $\tilde{E}=0.26$.

transformation to the normal modes of the system diagonalizes the Hamiltonian and yields an equidistant spacing of the eigenvalues [47]. In the local-mode limit—i.e., $\lambda\to 0$—the eigenvalues of $\hat{H}_0$ are obtained immediately from (1) and are partly degenerate.[3] However, in an intermediate-λ regime one observes a different behavior: namely, irregular evolution and level repulsion (see inset). This is a manifestation of the classically chaotic behavior [60,61].

In order to establish this statement, we turn to the statistical properties of the spectra. In particular, we will study the level spacing distribution $\mathcal{P}(S)$ [47,48,59,53] where

$$S_n=\frac{E_{n+1}-E_n}{\Delta} \tag{11}$$

are the spacings of two consecutive energy levels which are *unfolded* with respect to the local mean level spacing Δ. The level spacing distribution represents one of the most popular measures used in quantum chaos studies [61,60]. It turns out that the sub-$\hbar$ statistical features of the energy spectrum of chaotic systems are "universal" and obey the RMT predictions [62,63]. In contrast, nonuniversal, i.e., system-specific, features are reflected only in the large-scale properties of the spectrum and constitute the fingerprints of the underlying classical dynamics.

The mean level spacing Δ can be estimated from the fact that $\mathcal{N}\propto N^2$ levels span an energy window $\Delta E\propto\tilde{U}N\tilde{E}$, around some specific energy $\tilde{E}$ [see Eq. (1)]. Our considerations indicate the scaling relation

$$\Delta\approx 1.5\frac{\tilde{U}}{N}, \tag{12}$$

where the proportionality factor was found by a direct fit of our spectral data in the energy window around $\tilde{E}=0.26$ [29].

For chaotic systems the level spacing distribution $\mathcal{P}(S)$ follows the so-called *Wigner surmise* [61,64]

$$\mathcal{P}_{\rm ch}(S)=\frac{\pi}{2}Se^{-(\pi/4)S^2}, \tag{13}$$

indicating that there is a linear repulsion between nearby levels. Instead, for generic integrable systems there is no correlation between the eigenvalues and the distribution $\mathcal{P}(S)$ is Poissonian:

$$\mathcal{P}_{\rm int}(S)=e^{-S}. \tag{14}$$

In Fig. 4 we report some representative $\mathcal{P}(S)$ for levels in the energy window around $\tilde{E}=0.26$.[4] One observes a qualitative change in the shape of $\mathcal{P}(S)$ from Poissonian-like associated with very small and large λ values to Wigner-like for intermediate values of λ.

In order to quantify the degree of level repulsion (and thus of chaoticity), various phenomenological formulas for $\mathcal{P}(S)$ have been suggested that interpolate between the two limiting cases (13, 14) (see, for example, [65,66]). Here we use the so-called Brody distribution [66] given by the expression

$$\mathcal{P}_q(S)=\alpha S^q e^{-\beta S^{1+q}}, \tag{15}$$

where $\alpha=(1+q)\beta$, $\beta=\Gamma^{1+q}[(2+q)/(1+q)]$, and Γ is the gamma function. The two parameters α and β are determined by the condition that the distribution be normalized with a mean equal to 1 [67]. The so-called Brody parameter q is then obtained from direct fitting of $\mathcal{P}_q(S)$ to the numerically evaluated level spacing distribution. One readily verifies that for $q=0$, the distribution $\mathcal{P}_q(S)$ is Poissonian (14), while for $q=1$ it takes the form of (13).

The fitted values of the Brody parameter q for various λ's are summarized in Fig. 5. We see that for very small and very large λ the Brody parameter is small, indicating classically regular motion, while for intermediate values $0.04<\lambda$

[3]We note that these are "accidental" degeneracies. In contrast, systematic degeneracies resulting from the symmetry of the model are eliminated by restricting the calculations to the symmetric subspace [47]. See also the following footnote.

[4]We note that for level spacing distribution it is essential [61] to distinguish levels from different symmetry classes. Here, the statistics is performed over the symmetric singlet states of the BHH. See also Ref. [47].

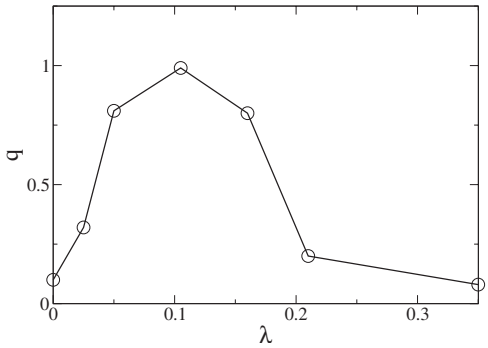

FIG. 5. The Brody parameter q for the BHH plotted against the dimensionless ratio λ, which controls the underlying classical dynamics. The values of q are obtained from fits to $P_q(S)$ around $\tilde{E}=0.26$ as reported in Fig. 4. Error bars are of the size of the circles. The system corresponds to $N=230$ bosons and $\tilde{U}=280$. See text for details.

<0.2 we find $q\sim 1$, corresponding to classically chaotic motion. This result is in perfect agreement with the predictions of the classical analysis.

B. Band profile

The fingerprints of classically chaotic dynamics can be found also in the band structure of the perturbation matrix **B**. As we will show below, the latter is related to the fluctuations of the classical motion. This is a major step towards a RMT modeling.

Consider a given ergodic trajectory $(I(\tilde{t}),\varphi(\tilde{t}))$ on the energy surface $\tilde{\mathcal{H}}(I(0),\varphi(0);k_0)=\tilde{E}$ (with $N=$const). We can associate with it a stochasticlike variable

$$\tilde{\mathcal{F}}(\tilde{t}) = -\frac{\partial \tilde{\mathcal{H}}}{\partial k}(I(\tilde{t}),\varphi(\tilde{t});k(\tilde{t})), \tag{16}$$

which can be seen as a generalized force. For the BHH (5) this is simply given by the perturbation term—i.e.,

$$\tilde{\mathcal{F}} = \sum_{i\neq j} \sqrt{I_i I_j} e^{i(\varphi_j-\varphi_i)}, \tag{17}$$

which corresponds to a *momentum boost* since it changes the kinetic energy [68]. It may have a nonzero average—i.e., a "conservative" part—but below we are interested only in its fluctuations.

In order to characterize the fluctuations of $\tilde{\mathcal{F}}(\tilde{t})$, we introduce the autocorrelation function

$$C(\tilde{\tau}) = \langle \tilde{\mathcal{F}}(\tilde{t})\tilde{\mathcal{F}}(\tilde{t}+\tilde{\tau})\rangle - \langle \tilde{\mathcal{F}}^2\rangle, \tag{18}$$

where $\tilde{\tau}=\tilde{U}\tau$ is a rescaled time. The angular brackets denote an averaging which is either microcanonical over some initial conditions $(I(0),\varphi(0))$ or temporal due to the assumed ergodicity.

For generic chaotic systems (with smoothly varying potentials), the fluctuations are characterized by a short correlation time $\tilde{\tau}_{\rm cl}$, after which the correlations are negligible. In generic circumstances $\tilde{\tau}_{\rm cl}$ is essentially the ergodic time. For our system we have found $\tilde{\tau}_{\rm cl}\sim 2\pi$ [see Eq. (20)].

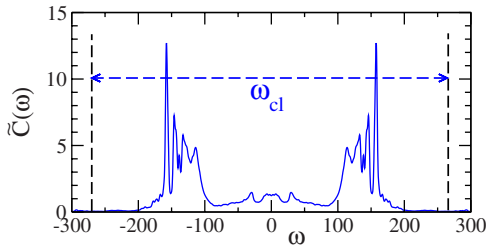

FIG. 6. (Color online) The power spectrum of the classical trimer (2) at energy $\tilde{E}=0.26$, $\tilde{U}=280$, and $\lambda_0=0.053$. The classical cutoff frequency $\omega_{\rm cl}=\tilde{\omega}_{\rm cl}\tilde{U}\approx 280$ is indicated by vertical dashed lines.

The power spectrum of the fluctuations $\tilde{C}(\tilde{\omega})$ is given by a Fourier transform:

$$\tilde{C}(\tilde{\omega}) = \int_{-\infty}^{\infty} C(\tilde{\tau}) e^{i\tilde{\omega}\tilde{\tau}} d\tilde{\tau}, \tag{19}$$

and for the case of the trimer (2) is shown in Fig. 6. We see that $\tilde{C}(\omega)$ has a (continuous) frequency support, which is bounded by $\tilde{\omega}_{\rm cl}\approx 1$, corresponding to $\omega_{\rm cl}\approx 280$ (indicated by dashed vertical lines in Fig. 6). The cutoff frequency $\omega_{\rm cl}$ is inversely proportional to the classical correlation time—i.e.,

$$\tilde{\omega}_{\rm cl} = \frac{2\pi}{\tilde{\tau}_{\rm cl}}. \tag{20}$$

These characteristics of the power spectrum are *universal* for generic chaotic systems. Finally, we see that within the frequency support the power spectrum $\tilde{C}(\tilde{\omega})$ is structured, reflecting *system-specific* properties of the underlying classical dynamics.

The classical power spectrum $\tilde{C}(\tilde{\omega})$ is associated with the quantum-mechanical perturbation matrix **B** according to the semiclassical relation [69,70]

$$\sigma_{nm}^2 \equiv \langle |\mathbf{B}_{nm}|^2\rangle = \frac{N^2\Delta}{\tilde{U}2\pi}\tilde{C}\left(\omega=\frac{E_n-E_m}{\hbar}\right). \tag{21}$$

Hence the matrix elements of the perturbation matrix **B** are extremely small outside a band of width

$$b = \hbar\omega_{\rm cl}/\Delta \approx \hbar\omega_{\rm cl}N/\tilde{U}. \tag{22}$$

In the inset of Fig. 7 we show a snapshot of the perturbation matrix $|\mathbf{B}_{nm}|^2$, which clearly exhibits a band structure. In the same figure we also display the scaled quantum band profile for $N=230$. The agreement with the classical power spectrum $\tilde{C}(\omega)$ is excellent. We have checked that the relation (21) is very robust [19,29,54] and holds even for a moderate number of bosons $N\approx 50$. Combining Eqs. (12) and (22) with $\tilde{\omega}_{\rm cl}\approx 1$ (see above) and the definition of b, we find for the chaotic regime around $\tilde{E}=0.26$ that $b\sim 0.6N$, which is confirmed by the numerics.

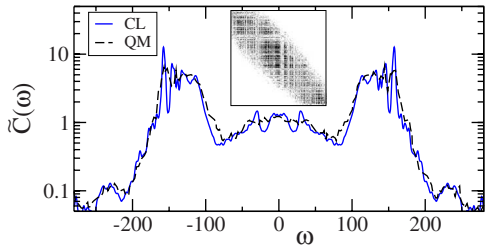

FIG. 7. (Color online) The band profile $(2\pi\tilde{U}/N^2\Delta)|\mathbf{B}_{nm}|^2$ versus $\omega=(E_n-E_m)/\hbar$ is compared with the classical power spectrum $\tilde{C}(\omega)$. The number of particles is $N=230$ and $\lambda_0=0.053$. Inset: a snapshot of the perturbation matrix $\mathbf{B}_{nm}$.

It is important to realize that upon quantization we end up with two distinct energy scales [19,29,54]. One is obviously the mean level spacing $\Delta\sim 1/N$ [see Eq. (12)], which is associated with the unperturbed Hamiltonian. The other energy scale is the bandwidth

$$\Delta_b = b\Delta \propto \tilde{U}, \tag{23}$$

which contains information about the power spectrum of the chaotic motion and is encoded in the perturbation matrix **B**. The latter energy scale is also known in the corresponding literature as the "nonuniversal" energy scale [71], or in the case of diffusive motion, as the Thouless energy [72]. One has to notice that deep in the semiclassical regime $N\to\infty$ these two energy scales differ enormously from one another. We shall see in the following sections that this scale separation has dramatic consequences on the theory of wave-packet dynamics.

C. Distribution of matrix elements of the perturbation operator

We further investigate the statistical properties of the matrix elements $\mathbf{B}_{nm}$ of the perturbation matrix by studying their distribution. RMT assumes that upon appropriate "unfolding" they must be distributed in a Gaussian manner. The unfolding aims to remove system-specific properties and to reveal the underlying universality. It is carried out by normalizing the matrix elements with the local standard deviation $\sigma=\sqrt{\langle|\mathbf{B}_{nm}|^2\rangle}$ related through Eq. (21) with the classical power spectrum $\tilde{C}(\omega)$.

The existing literature is not conclusive about the distribution of the normalized matrix elements $w=\mathbf{B}_{nm}/\sigma$. Specifically, Berry [73] and more recently Prosen and Robnik [70,74] claimed that $\mathcal{P}(w)$ should be Gaussian. On the other hand, Austin and Wilkinson [75] have found that the Gaussian is approached only in the limit of high quantum numbers, while for small numbers—i.e., low energies—a different distribution applies: namely,

$$P_{\text{couplings}}(w) = \frac{\Gamma\left(\frac{N}{2}\right)}{\sqrt{\pi N}\Gamma\left(\frac{N-1}{2}\right)}\left(1-\frac{w^2}{N}\right)^{(N-3)/2}. \tag{24}$$

This is the distribution of the elements of an N-dimensional vector, distributed randomly over the surface of an N-dimensional sphere of radius $\sqrt{N}$. For $N\to\infty$ this distribution approaches a Gaussian.

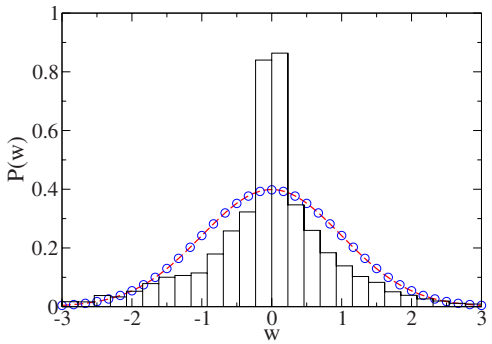

FIG. 8. (Color online) Distribution of rescaled matrix elements w around $\tilde{E}=0.26$ rescaled with the averaged band profile. The dashed red line corresponds to the standard normal distribution, while the circles (○) correspond to a best fit from Eq. (24) with a fitting parameter $N=342$. The system corresponds $N=230$, $\tilde{U}=280$.

In Fig. 8 we report the distribution $\mathcal{P}(w)$ for the elements of the perturbation matrix **B**. The dashed line corresponds to a Gaussian of unit variance, while the circles are obtained by fitting Eq. (24) to the numerical data using N as a fitting parameter. Although we are deep in the semiclassical regime (i.e., $N=230$), none of the above predictions describes in a satisfactory way the numerical data. We attribute these deviations to the existence of small stability islands in the phase space. Trajectories started in those islands cannot reach the chaotic sea and vice versa. Quantum mechanically, the consequence of this would be vanishing matrix elements $\mathbf{B}_{nm}$, which represent the classically forbidden transitions.

D. RMT modeling

More than 50 years ago, Wigner [62,63] proposed a simplified model to study the statistical properties of eigenvalues and eigenfunctions of complex systems. It is known as the *Wigner banded random matrix* (WBRM) model. The corresponding Hamiltonian is given by Eq. (5) where **B** is a *banded random* matrix [76–78]. This approach is attractive both analytically and numerically. Analytical calculations are greatly simplified by the assumption that the off-diagonal terms can be treated as independent random numbers. Also from a numerical point of view it is quite a tough task to calculate the true matrix elements of **B**. It requires a preliminary step where $\hat{H}_0$ is diagonalized. Due to memory limitations, one ends up with quite small matrices. For example, for the Bose-Hubbard Hamiltonian we were able to handle matrices of final size $\mathcal{N}=30\,000$ maximum. This should be contrasted with RMT simulations, where using a self-expanding algorithm [19,27,79] we were able to handle system sizes up to $\mathcal{N}=1\,000\,000$ along with significantly reduced CPU time. We would like to stress, however, that the underlying assumption of the WBRM—namely, that the off-diagonal elements are *uncorrelated* random numbers—has to be treated with extreme care. The applicability of this model is therefore a matter of conjecture, which we will test in the following sections.

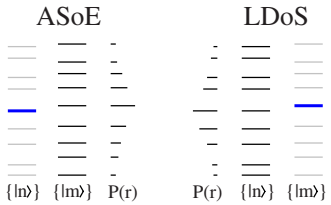

FIG. 9. (Color online) Schematic representation of the two notions of the kernel $P(n|m)$. Left: projection of one perturbed eigenstate $|n(k_0+\delta k)\rangle$ (bold blue level) on the basis $|m(k_0)\rangle$ of the unperturbed Hamiltonian. Averaging over several $|n'\rangle$ states around energy E_n yields the averaged shape of eigenfunctions (ASOE). Right: alternatively, if $P(n|m)$ is regarded as a projection of one unperturbed eigenstate $|m\rangle$ (bold blue level) on the basis $|n\rangle$ of the perturbed Hamiltonian and averaged over several states around E_m, it leads to the local density of states (LDOS).

In fact, the WBRM model involves an additional simplification. Namely, one assumes that the perturbation matrix **B** has a *rectangular* band profile of bandwidth b. A simple inspection of the band profile of our BHH model (see Fig. 7) shows that this is not the case. We eliminate this simplification by introducing a RMT model that is even closer to the dynamical one. Specifically, we generate the matrix elements B_{nm} from a Gaussian distribution with a variance that is given by the classical power spectrum according to Eq. (21). Thus the band structure is kept intact. This procedure leads to a random model that exhibits only universal properties, but lacks any classical limit. We will refer to it as the *improved* random matrix theory model (IRMT).

V. LOCAL DENSITY OF STATES AND QUANTUM-CLASSICAL CORRESPONDENCE

As we change the parameter δk in the Hamiltonian (5), the instantaneous eigenstates $\{|n(k)\rangle\}$ undergo structural changes. Understanding these changes is a crucial step towards the analysis of wave-packet dynamics [29,54]. This leads to the introduction of the "kernel"

$$P(n|m) = |\langle n(k_0+\delta k)|m(k_0)\rangle|^2, \tag{25}$$

which can be interpreted in two ways as we schematically depict in Fig. 9. If regarded as a function of m, $P(n|m)$ represents the overlap of a given perturbed eigenstate $|n(k_0+\delta k)\rangle$ with the eigenstates $|m(k_0)\rangle$ of the unperturbed Hamiltonian. The averaged distribution $P(r)$ is defined by $r=n-m$, and averaging over several states with roughly the same energy E_n yields the averaged shape of eigenfunctions (ASOE). Alternatively, if regarded as a function of n and averaging over several states around a given energy E_m, the kernel $P(r)$ represents up to some trivial scaling and shifting the LDOS:

$$P(E|m) = \sum_n |\langle n(k)|m(k_0)\rangle|^2 \delta(E-E_n). \tag{26}$$

Its line shape is fundamental for the understanding of the associated dynamics (see Sec. VI), since its Fourier transform is the so-called "survival probability amplitude." In the following we will focus on the LDOS scenario.

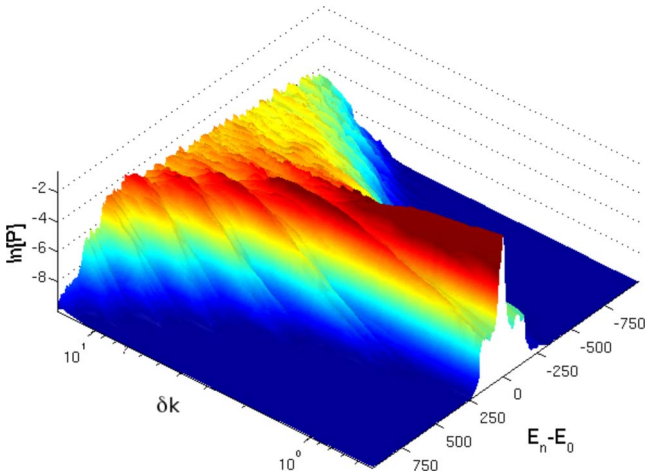

FIG. 10. (Color online) The kernel $P(n|m)$ of the BHH plotted as a function of the perturbed energies E_n (LDOS representation) and for various perturbation strengths $\delta k > \delta k_{\rm qm}$. The averaged shape of eigenfunctions is given by the same kernel $P(n|m)$ and is obtained by just inverting the energy axis. Here, $N=70$, and $\lambda_0 = 0.053$.

A. Parametric evolution of the LDOS

An overview of the parametric evolution of the averaged $P(n|m)$ is shown in Fig. 10 [29]. Beginning as a delta function for $\delta k=0$, the profile $P(n|m)$ starts to develop a nonperturbative core as δk increases above some critical value $\delta k_{\rm qm}$. For even stronger perturbations, $P(n|m)$ spills over the entire bandwidth Δ_b. We will show that if δk exceeds another critical value $\delta k_{\rm prt}$, the LDOS develops classical features. In the following we will identify the above parametric regimes and discuss the theory of $P(n|m)$ in each one of them.

1. Perturbative regimes

We start with the discussion of the perturbative regimes. We distinguish between two cases.

Standard perturbative regime. The simplest case is obviously the first-order perturbation theory (FOPT) regime where, for $P(n|m)$, we can use the standard textbook approximation $P_{\rm FOPT}(n|m) \approx 1$ for $n=m$, while

$$P_{\rm FOPT}(n|m) = \frac{\delta k^2 |\mathbf{B}_{mn}|^2}{(E_n - E_m)^2} \tag{27}$$

for $n \neq m$. The border $\delta k_{\rm qm}$ for which Eq. (27) describes the LDOS kernel can be found by the requirement that only nearest-neighbor levels be mixed by the perturbation. We get

$$\delta k_{\rm qm} = \Delta/\sigma \propto \frac{\tilde{U}}{N^{3/2}}, \tag{28}$$

where for the right-hand side of Eq. (28) we have used the scaling relations for Δ and σ [see Eqs. (12) and (21)]. In Fig. 11(a) we report our numerical results for the BHH, together

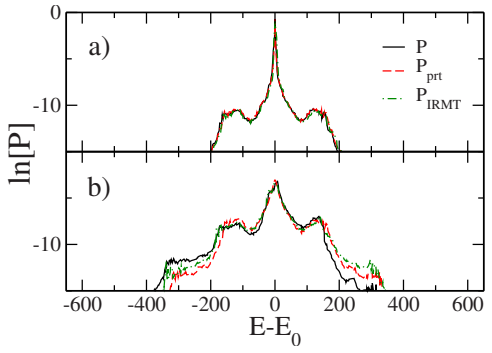

FIG. 11. (Color online) The quantal profile $P(n|m)$ (solid black line) as a function of $E_n - E_m^{(0)}$ for the BHH model is compared with $P_{\rm prt}$ (dashed red line) and with the corresponding $P_{\rm IRMT}$ (dash-dotted green line) of the IRMT model. The perturbation strength δk is in (a) standard perturbative regime $\delta k = 0.05$ and (b) extended perturbative regime $\delta k = 0.3$. The system corresponds to $N = 230$, $\tilde{U} = 280$, and $k_0 = 15$. Here $\delta k_{\rm qm} = 0.09$ and $\delta k_{\rm prt} = 1.02$.

with the perturbative profile $P_{\rm FOPT}(n|m)$ obtained from Eq. (27) and the outcome of the IRMT modeling. The FOPT, Eq. (27), has as an input the classical power spectrum $\tilde{C}(\omega)$, which via Eq. (21) can be used in order to evaluate the band profile $\mathbf{B}_{nm}$. All three curves fall on top of one another.

Extended perturbative regime. If $\delta k > \delta k_{\rm qm}$, but not too large, then we expect that several levels are mixed nonperturbatively. This leads to a distinction between a "core" of width Γ which contains most of the probability and a tail region which is still described by FOPT. This nontrivial observation can be justified using perturbation theory to infinite order. It turns out that the nonperturbative mixing on the small scale Γ of the core does not affect the long-range transitions [54,80] that dictate the tails. Therefore we can argue that a reasonable approximation is [54]

$$P_{\rm prt}(n|m) = \frac{\delta k^2 |\mathbf{B}_{mn}|^2}{(E_n - E_m)^2 + \Gamma^2}. \tag{29}$$

Our numerical data, reported in Fig. 11(b), indicate again an excellent agreement with the theoretical prediction (29). At the same time, we observe that also the proposed IRMT describes quite nicely the actual profile $P(r)$. Note that the resulting line shape is strikingly different from a Wigner Lorentzian (as predicted by the traditional RMT modeling) and is rather governed by the semiclassical structures of the band profile $|\mathbf{B}_{nm}|^2$. Instead, a Wigner Lorentzian would be obtained if the band profile of the perturbation matrix were flat.

The core width Γ is evaluated by imposing normalization on $P_{\rm prt}(n|m)$ [29]. Our numerically evaluated Γ is reported in Fig. 12. We see that for very small δk we get that $\Gamma \ll \Delta$. In this case, the expression (29) collapses to the FOPT expression (27). In fact, the inequality $\Gamma \leqslant \Delta$ can be used in order to estimate the limit $\delta k_{\rm qm}$ of the validity of FOPT. As soon as we enter the extended perturbative regime, we find (see Fig. 12) that Γ grows as

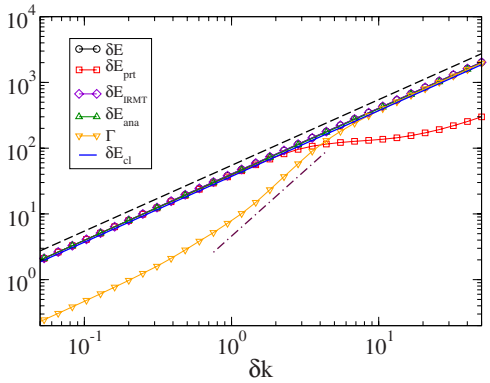

FIG. 12. (Color online) Various measures of the spreading profile for the BHH and IRMT models: the quantal spreading δE (black line with ○), the quantal spreading $\delta E_{\rm prt}$ of the perturbative profile given by Eq. (29) (red line with □), the spreading $\delta E_{\rm IRMT}$ (violet line with ◇) obtained from the IRMT modeling, the analytical spreading $\delta E_{\rm ana}$ (green line with △) obtained from (34), the core-width Γ (orange line with ▽), and the classical spreading $\delta E_{\rm cl}$ (blue line). The dashed line has slope 1, while the dash-dotted line has slope 2 and are drawn to guide the eye. The systems correspond to $N = 70$ bosons, $k_0 = 15$, and $\tilde{U} = 280$. See text for details.

$$\Gamma \propto \left(\delta k \frac{\sigma}{\Delta}\right)^2 \Delta. \tag{30}$$

The core width Γ [and thus Eq. (29) for the LDOS] is meaningful only as long as we have $\Gamma < \Delta_b$—i.e., as long as we can distinguish a core-tail structure. This condition allows us to evaluate the perturbative border $\delta k_{\rm prt}$:

$$\delta k_{\rm prt} \propto \frac{\tilde{U}}{N}. \tag{31}$$

In our numerical analysis we have defined $\delta k_{\rm qm}$ as the perturbation strength for which 50% of the probability remains at the original site, but we have checked that the condition $\Gamma = \Delta$ gives the same result. For determining $\delta k_{\rm prt}$ we use the following numerical procedure: We calculate the spreading $\delta E = \sqrt{\Sigma_n P(n|m)(E_m^{(0)} - E_n)^2}$ of $P(r)$. Next we calculate $\delta E_{\rm prt}(\delta k)$, using Eq. (29). This quantity always saturates for large δk because of having a finite bandwidth. We compare it to the exact $\delta E(\delta k)$ and define $\delta k_{\rm prt}$, for instance, as the 80% departure point. In Fig. 13, we present our numerical data for $\delta k_{\rm qm}$ and $\delta k_{\rm prt}$ by making use of the scaling

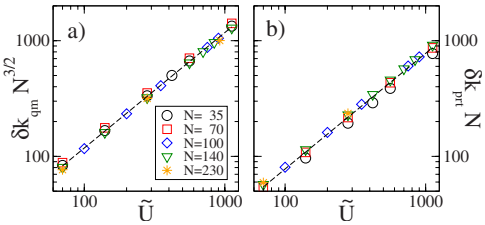

FIG. 13. (Color online) The parameters (a) $\delta k_{\rm qm}$ and (b) $\delta k_{\rm prt}$ for various $\tilde{U}$, N, and for $\lambda_0 = 0.053$. A nice scaling in accordance with Eqs. (28) and (31) is observed.

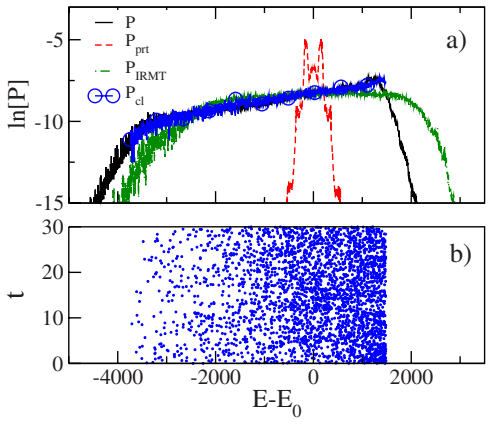

FIG. 14. (Color online) Upper panel: the kernel $P(n|m)$ (LDOS representation) in the nonperturbative regime $\delta k=10$ for $N=230$ and $\lambda=0.053$. The results of the BHH model (solid black line) are compared with P_{prt} (red dashed line), P_{IRMT} of the IRMT model (dash-dotted green line), and the classical profile P_{cl} (blue line with ○). Lower panel: a time series $E(t)$ which leads to the classical profile $P_{\mathrm{cl}}(E)$ (see text for details).

relations (28) and (31). A nice overlap is evident, confirming the validity of the above expressions.

2. Nonperturbative regime

For $\delta k > \delta k_{\mathrm{prt}}$ the core spills over the bandwidth and therefore perturbation theory, even to infinite order, is inapplicable for evaluating $P(n|m)$. In this regime, we observe that also the IRMT fails to reproduce the actual line shape of $P(n|m)$ as can be seen from Fig. 14(a). In fact, RMT modeling leads to a semicircle

$$P(n|m) = 1/(2\pi\Delta)\sqrt{4-[(E_n-E_m)/\Delta]^2}, \tag{32}$$

as predicted by Wigner [62].

What is the physics behind the LDOS line shape in the nonperturbative regime? Due to the strong perturbations, many levels are mixed and hence the quantum nature becomes "blurred." Then, we can approximate the spreading profile by the semiclassical expression [54,80,81]

$$P_{\mathrm{sc}}(n|m) = \int \frac{dId\varphi}{(2\pi\hbar)^d}\rho_n(I,\varphi)\rho_m(I,\varphi), \tag{33}$$

where $\rho_m(I,\varphi)$ and $\rho_n(I,\varphi)$ are the Wigner functions that correspond to the eigenstates $|m(k_0)\rangle$ and $|n(k)\rangle$, respectively. In the strict classical limit, ρ can be approximated by the corresponding microcanonical distribution $\rho \propto \delta(E-\mathcal{H}(\{I_i\},\{\varphi_i\}))$ determined by the energy surface E. The latter can be evaluated by projecting the dynamics generated by $\mathcal{H}_0(\{I_i\},\{\varphi_i\})=E_0$ onto the Hamiltonian $\mathcal{H}(\{I_i\},\{\varphi_i\})=E(t)$.

In Fig. 14(b) we plot the resulting $E(t)=\mathcal{H}(I(t),\varphi(t))$ as a function of time for the Hamiltonian (2). The classical distribution $P_{\mathrm{cl}}(n|m)$ is constructed [Fig. 14(a)] from $E(t)$ by averaging over a sufficiently long time. The good agreement with the quantum profile $P(n|m)$ is a manifestation of the detailed quantum-classical correspondence which affects the whole LDOS profile in the nonperturbative regime.

Coming back to the failure of the IRMT approach, we are now able to understand it formally from the scaling relation (31) of the perturbative border $\delta k_{\mathrm{prt}} \sim \tilde{U}/N$. Specifically, we observe that the nonperturbative limit can be approached either by increasing the perturbation strength δk or, alternatively, by keeping δk constant and increasing N. As we have seen before, increasing N means to approach the classical limit (keeping $\tilde{U}=$const). On the other hand, it is clear that the IRMT model lacks a classical limit. Therefore, we cannot expect it to yield a correct description of $P(n|m)$ in that regime. Instead, for $\delta k > \delta k_{\mathrm{prt}}$ the LDOS is completely dictated by semiclassical considerations as can be seen from Fig. 14(a).

B. Restricted vs detailed quantum-classical correspondence

It is important to distinguish between detailed and restricted QCC [18,82]. The two types of QCC are defined as follows: (a) detailed QCC means $P(r) \approx P_{\mathrm{cl}}(r)$, while (b) restricted QCC means $\delta E_{\mathrm{qm}} \approx \delta E_{\mathrm{cl}}$.

Obviously restricted QCC is a trivial consequence of detailed QCC, but the converse is not true. It turns out that restricted QCC is much more robust than detailed QCC. In Fig. 12 we see that the dispersion δE_{qm} of either $P(r)$ or $P_{\mathrm{IRMT}}(r)$ is almost indistinguishable from δE_{cl}. In fact, this agreement of the second moment δE persists also for the case of the perturbative profile (29). This is quite remarkable because the corresponding LDOS profiles (quantal, perturbative, IRMT, and classical) can become very different!

The possibility of having restricted QCC was pointed out in [54,81] in the framework of quantum systems with chaotic classical limit. A simple proof presented in Ref. [54] indicated that the variance of $P(r)$ is determined by the first two moments of the Hamiltonian in the unperturbed basis—i.e.,

$$\begin{aligned}\delta E^2 &= \langle m|\hat{H}^2|m\rangle - \langle m|\hat{H}|m\rangle^2 \\ &= \delta k^2[\langle m|\hat{B}^2|m\rangle - \langle m|\hat{B}|m\rangle^2] \\ &= \delta k^2\left[\sum_n |\mathbf{B}_{nm}|^2 - |\mathbf{B}_{mm}|^2\right].\end{aligned} \tag{34}$$

Having a δE_{qm} that is determined only by the band profile is the reason for restricted QCC and is also the reason why restricted QCC is not sensitive to the RMT assumption.

VI. WAVE-PACKET DYNAMICS

We now turn to the time-dependent scenario of the wave-packet dynamics which is related to the response of a system to a rectangular pulse. Its physical realization in the framework of the BHH has been described in Sec. III.

In the next subsections we will discuss the time-evolving energy profile in each of the three δk regimes which we have identified in the framework of the LDOS study. We start our analysis with the classical dynamics (Sec. VI A) and then turn to the evolution of the quantum profile $P_t(r)$ (Sec. VI B). In the same subsection we will present an analysis of the IRMT and semiclassical modeling and identify both their weakness and regimes of validity.

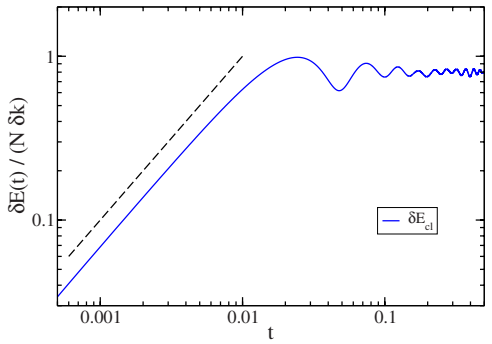

FIG. 15. (Color online) The classical energy spreading $\delta E_{\rm cl}(t)$ for the BHH (normalized with respect to the perturbation strength δk and the boson number N) is plotted as a function of time. The dashed line has slope one and is drawn to guide the eye.

A. Classical dynamics

The classical picture is quite clear: The initial preparation is assumed to be a microcanonical distribution that is supported by the energy surface $\mathcal{H}_0(I,\varphi)=E(0)=E_{n_0}$, where the Hamiltonian is given by Eq. (2). Taking $\mathcal{H}(\lambda)$ to be a generator for the classical dynamics, the phase-space distribution spreads away from the initial surface for $t>0$. "Points" of the evolving distribution move upon the energy surfaces of $\mathcal{H}(I,\varphi)$. Thus, the energy $E(t)=\mathcal{H}_0(I(t),\varphi(t))$ of the evolving distribution spreads with time. We are interested in the distribution of $E(t)$ of the evolving "points."

A quantitative description of the classical spreading is easily obtained from Hamilton's equations:

$$\frac{dE(t)}{dt}=[\mathcal{H},\mathcal{H}]_{\rm PB}+\frac{\partial\mathcal{H}}{\partial t}=-\delta k\dot{f}(t)\mathcal{F}(t), \tag{35}$$

where $[\cdot]_{\rm PB}$ indicates the Poisson brackets and $f(t)$ is a rectangular pulse—i.e., $f(t')=1$ for $0<t'<t$. Integrating the previous expression and then taking a microcanonical average over initial conditions, we get for the energy spreading the classical LRT expression

$$\delta E_{\rm cl}(t)=\delta k\sqrt{2[C(0)-C(t)]}\approx\begin{cases}\delta E_{\rm cl}\dfrac{t}{\tau_{\rm cl}}, & t<\tau_{\rm cl},\\ \delta E_{\rm cl}, & t>\tau_{\rm cl}.\end{cases} \tag{36}$$

In the last step, we have expanded the correlation function for $t\ll\tau_{\rm cl}$ as $C(t)\approx C(0)-\frac{1}{2}C''(0)t^2$. For $t\gg\tau_{\rm cl}$, due to ergodicity, a "steady-state distribution" appears, where the evolving "points" occupy an "energy shell" in phase space. The thickness of this energy shell equals $\delta E_{\rm cl}$. Thus, the classical dynamics is fully characterized by the two classical parameters $\tau_{\rm cl}$ and $\delta E_{\rm cl}$.

Figure 15 shows the scaled classical energy spreading $\delta E_{\rm cl}(t)/(N\delta k)$ for the BHH. The heavy dashed line has slope 1 and is drawn to guide the eye. In agreement with Eq. (36) we see that $\delta E_{\rm cl}(t)$ is first ballistic and then saturates at $\tau_{\rm cl}\approx 2\pi/\tilde{U}=0.02$.

One can also calculate the entire classical evolving profile $P_{\rm cl}(t)$. Using a phase-space approach similarly to the LDOS case in Sec. V A 2, we propagate, up to time t under the Hamiltonian $\mathcal{H}$, a large set of trajectories $\{E\}_{t=0}$ that originally are supported by the energy surface $\mathcal{H}_0(I,\varphi)=E(t=0)=E_{n_0}$. Projecting them back onto $\mathcal{H}_0$ yields a set of energies $\{E\}_{t=t}$ whose distribution[5] constitutes the spreading profile $P_{\rm cl}(t)$ at time t. We will discuss $P_{\rm cl}(t)$ in Sec. VI C.

B. Quantum dynamics

Now we would like to explore the various dynamical scenarios that are generated by the Schrödinger equation for $a_n(t)=\langle n|\psi(t)\rangle$. Namely, we want to solve

$$\frac{da_n}{dt}=-\frac{i}{\hbar}E_n a_n-\frac{i}{\hbar}\sum_m \mathbf{B}_{nm}a_m, \tag{37}$$

starting with an initial preparation $a_n=\delta_{nm}$ at $t=0$—i.e., an eigenstate of the unperturbed system. We describe the energy-spreading profile for $t>0$ by the transition probability kernel $P_t(n|m)=\langle|a_n(t)|^2\rangle$. The angular brackets stand for averaging over initial states (m) belonging to the energy interval $0.25\leqslant\tilde{E}_m\leqslant 0.27$. We characterize the evolving distribution using the various measures introduced in Sec. III A. If the evolution is classical-like, then, according to the classical analysis presented previously, $P_t(n|m)$ will be characterized by a single energy scale $\delta E(t)$, meaning that any other measure like $\delta E_{\rm core}(t)$ reduces (up to a numerical factor) to $\delta E(t)$. We will use this criterion in the following in order to identify for which δk regimes the evolution is classical-like and for which ones it develops quantum features.

An overview of the spreading profiles for three representative δk strengths is given in Fig. 16. A qualitative difference in the spreading is evident: In Fig. 16(a) the probability is mainly concentrated in the initial level for all times (standard perturbative regime). In Fig. 16(b) one can distinguish two different components in the $P_t(n|m)$—the "core" [characterized by $\delta E_{\rm core}(t)$] and the "tail" component [characterized by $\delta E(t)$]—both of them being smaller than the bandwidth (extended perturbative regime). For even stronger perturbations, the core spills all over the bandwidth [see Fig. 16(c)] and the dynamics is nonperturbative. In the following we discuss each of these regimes separately.

1. Perturbative regimes

For small perturbations $\delta k<\delta k_{\rm qm}$ [see Fig. 16(a)], the probability is mainly concentrated in the initial level during the *entire* evolution. This is the FOPT (standard perturbative) regime where the perturbation mixes only nearby levels and little probability escapes to the tails.

As the perturbation strength is increased, $\delta k_{\rm qm}<\delta k<\delta k_{\rm prt}$ [Fig. 16(b)], levels within the bandwidth are mixed and one can distinguish two different components in the profile $P_t(r)$: The core characterized by $\delta E_{\rm core}(t)$, where most of the probability is concentrated, and the tail component, characterized by $\delta E(t)$. The latter is reported in Fig. 17(a) to-

[5]Technically, this requires calculating the histogram with a bin size given by the mean level spacing Δ.

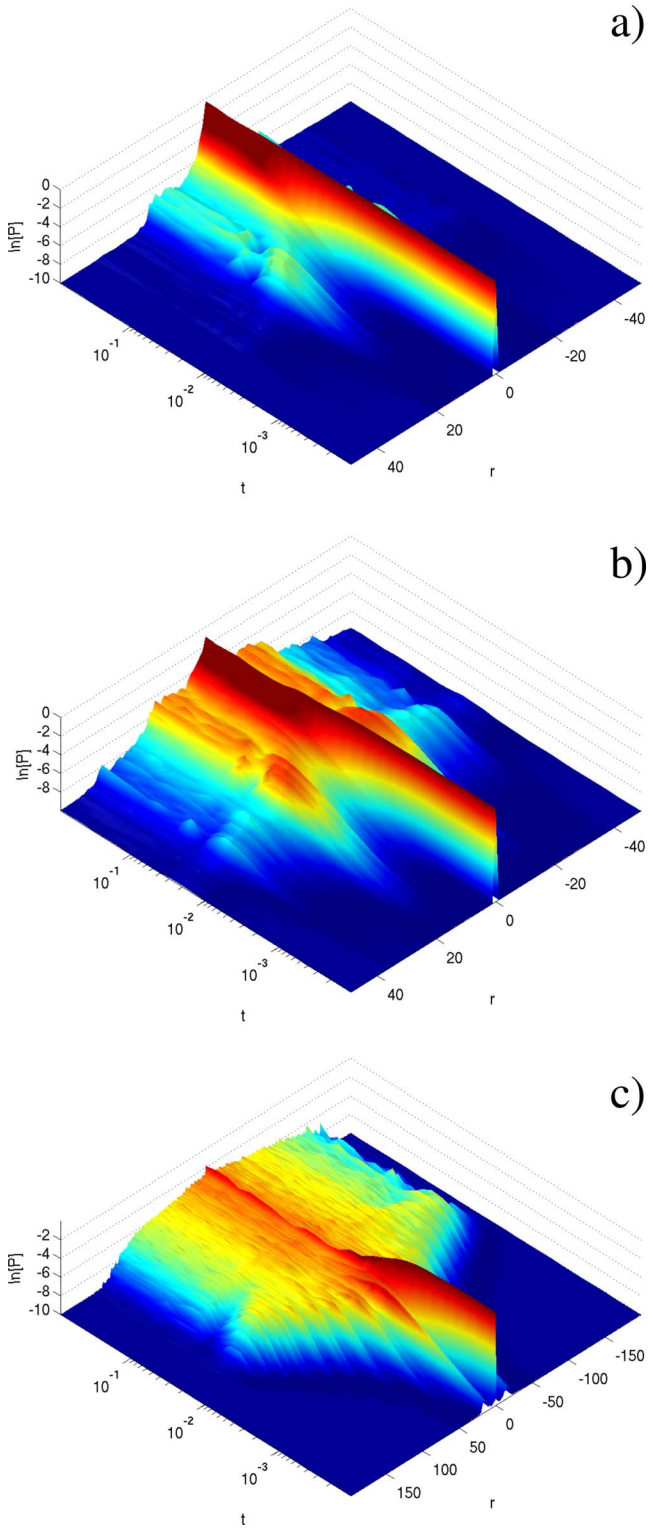

FIG. 16. (Color online) The profile $P_t(r)$ of the BHH plotted as a function of time for various perturbation strengths $\delta k < \delta k_{\mathrm{qm}}$ (a), $\delta k_{\mathrm{qm}} < \delta k < \delta k_{\mathrm{prt}}$ (b), and $\delta k > \delta k_{\mathrm{prt}}$ (c). Note the different scale in (c). Here, $N=70$, $\tilde{E}=0.26$ and $\lambda_0=0.053$.

gether with the classical spreading $\delta E_{\mathrm{cl}}(t)$. The remarkable fact is that, as far as $\delta E(t)$ is concerned, the agreement with the classical result is perfect. This might lead to the wrong impression that the classical and quantum spreading are of the same nature. However, this is definitely not the case.

In order to reveal the different nature of the quantum spreading in the perturbative regime we turn to the analysis of the core width $\delta E_{\mathrm{core}}(t)$ [see Fig. 17(b)]. If the spreading were of classical type, this would imply that the evolving profile would be characterized by a single energy scale, and thus $\delta E(t) \sim \delta E_{\mathrm{core}}(t)$. However, as can be seen in Fig. 17(b), this is certainly not the case: For $\delta k < \delta k_{\mathrm{qm}}$ we have that $\delta E_{\mathrm{core}}(t) = \Delta$ for all times while for $\delta k_{\mathrm{qm}} < \delta k < \delta k_{\mathrm{prt}}$ the core width fulfills the inequalities $\Delta < \delta E_{\mathrm{core}}(t) < \delta E(t) < \Delta_b$. In fact, this separation of energy scales allows us to use perturbation theory in order to evaluate theoretically the evolving second moment of the energy distribution. We get for the transition probability from an initial state m to any other state $n \neq m$

$$P_t(n|m) = \frac{\delta k^2}{\hbar^2} |\mathbf{B}_{nm}|^2 \frac{\tilde{F}_t(\omega_{nm})}{(\omega_{nm})^2}. \tag{38}$$

Here $\tilde{F}_t(\omega) = (\omega t)^2 \mathrm{sinc}^2(\omega t/2)$ is the spectral content of a constant perturbation of duration t and $\mathrm{sinc}(x) = \sin(x)/x$. Substituting the above expression into Eq. (9), we get the LRT expression (36) for $\delta E(t)$. We have also calculated the second moment resulting from the IRMT modeling. The outcome is reported in the inset of Fig. 17(a) and shows that within the perturbative regime the IRMT modeling provides the same results (as far as the second moment is concerned) as the LRT calculations. Therefore we conclude that for $\delta k \leqslant \delta k_{\mathrm{prt}}$ the IRMT modeling, the LRT results, the classical results δE_{cl}, and the quantum calculations for the second moment $\delta E(t)$ of the BHH match one another.

Encouraged by this success of LRT and IRMT modeling to describe the second moment $\delta E(t)$ of the energy spreading, we can further use them to evaluate the survival probability $\mathcal{P}(t)$. Assuming a Markovian picture of the dynamics, LRT predicts [19]

$$\mathcal{P}(t) = \exp\left[-\delta k^2 \int_{-\infty}^{\infty} \frac{d\omega}{2\pi} \tilde{C}(\omega) \frac{\tilde{F}_t(\omega)}{(\hbar\omega)^2} \right], \tag{39}$$

which after substituting the spectral content $\tilde{F}_t(\omega)$ can be rewritten in the form

$$\mathcal{P}(t) = \exp\left[-\left(\frac{\delta k}{\hbar}\right)^2 \int_{-\infty}^{\infty} \frac{d\omega}{2\pi} \tilde{C}(\omega) t t \, \mathrm{sinc}^2\left(\frac{\omega t}{2}\right) \right]. \tag{40}$$

For short times ($t \ll \tau_{\mathrm{cl}}$) during which the spreading is ballistic like, the term $t\mathrm{sinc}^2(\omega t/2)$ is broad compared to the band profile and can be approximated by t, leading to

$$\mathcal{P}(t) = \exp\left[-C(\tau=0)\left(\frac{\delta k t}{\hbar}\right)^2 \right]. \tag{41}$$

For longer times ($t \gg \tau_{\mathrm{cl}}$), on the other hand, the term $t\mathrm{sinc}^2(\omega t/2)$ is extremely narrow and can be approximated by a delta function $\delta(\omega)$. This results in a Fermi-golden-rule (FGR) decay

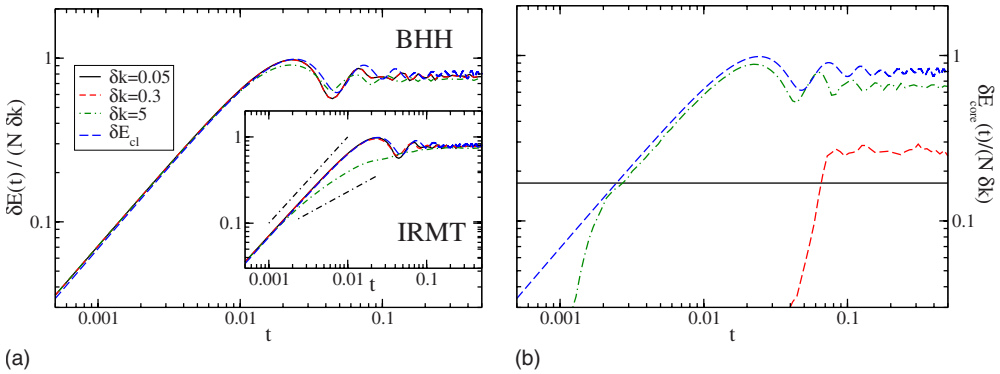

FIG. 17. (Color online) Left panel: the (normalized) energy spreading $\delta E(t)$ for the BHH and the IRMT model (inset) for three different perturbation strengths $\delta k=0.05<\delta k_{\mathrm{qm}}$ (solid black line), $\delta k_{\mathrm{qm}}<\delta k=0.3<\delta k_{\mathrm{prt}}$ (dashed red line), and $\delta k=5>\delta k_{\mathrm{prt}}$ (dash-dotted green line). The classical expectation $\delta E_{\mathrm{cl}}(t)$ is represented in all three plots by a dashed blue line for comparison. In the inset the black dash-dotted lines have slope 1 and $\frac{1}{2}$ respectively, and are drawn to guide the eye. While for the BHH model one observes restricted quantum-classical correspondence in all regimes, this is not the case for the IRMT model (inset): For perturbations $\delta k>\delta k_{\mathrm{prt}}$ the energy spreading $\delta E(t)$ exhibits a premature crossover to diffusive behavior. Right panel: the evolution of the corresponding core width $\delta E_{\mathrm{core}}(t)$ for the BHH model is plotted. In the perturbative regimes one observes a separation of scales $\delta E_{\mathrm{core}}(t)<\delta E(t)<\Delta_b$, which is lost for strong perturbations $\delta k>\delta k_{\mathrm{prt}}$, where $\delta E_{\mathrm{core}}(t)$ approaches more and more the classical expectation $\delta E_{\mathrm{cl}}(t)$. Here, $N=230$, $\tilde{U}=280$, $\tilde{E}=0.26$, and $\lambda_0=0.053$.

$$\mathcal{P}(t)=\exp\left[-\left(\frac{\delta k}{\hbar}\right)^2\tilde{C}(\omega=0)t\right], \tag{42}$$

which can be trusted as long as $\mathcal{P}(t)\sim 1$. This can be converted into an inequality $t<t_{\mathrm{prt}}=(\frac{\delta k_{\mathrm{prt}}}{\delta k})^2\tau_{\mathrm{cl}}$.

In Fig. 18(a) we plot our numerical results for the trimeric BHH model together with the theoretical expectation (39) (we note that the outcome of the IRMT modeling matches exactly the results of the LRT and thus we do not overplot them). In both perturbative regimes we observe a short initial Gaussian decay [as implied by Eq. (41)], which is followed by the exponential FGR decay. In the FOPT regime [inset of Fig. 18(a)] the entire decay until saturation is described by LRT. In the extended perturbative regime [see Fig. 18(a)], the overall agreement is still pretty good. However, here the perturbative break time t_{prt} is shorter and one finds a deviation around the time $t_{\mathrm{prt}}\sim 0.01$.

2. Nonperturbative regime

Once we enter the nonperturbative regime $\delta k>\delta k_{\mathrm{prt}}$ [see Fig. 16(c)], the core spills over the bandwidth and the separation of energy scales is lost, leading to $\delta E(t)\sim\delta E_{\mathrm{core}}(t)>\Delta_b$ [see Fig. 17(b) for $\delta k=5$]. In this case the evolving energy distribution becomes totally nonperturbative. Still, for short times $t_{\mathrm{prt}}=(\frac{\delta k_{\mathrm{prt}}}{\delta k})\tau_{\mathrm{cl}}<\tau_{\mathrm{cl}}$, defined by the requirement that $\mathcal{P}(t)\sim 1$ [see Eq. (41)], the evolving probability kernel $P_t(n|m)$ [and therefore the spreading $\delta E(t)$] is described accurately by the FOPT expression (38).

The remarkable fact is that although for $t>t_{\mathrm{prt}}$ the evolving profile $P(n|m)$ is totally nonperturbative, this crossover is *not* reflected in the variance [see Fig. 17(a)]. The agreement with the LRT results of Eq. (36) is still perfect. Instead, the crossover can be detected by studying other moments like $\delta E_{\mathrm{core}}(t)$, which acquire classical characteristics—i.e., $\delta E_{\mathrm{core}}(t)\approx\delta E(t)=\delta E_{\mathrm{cl}}(t)$ [see Fig. 17(b)]. Thus we are led to

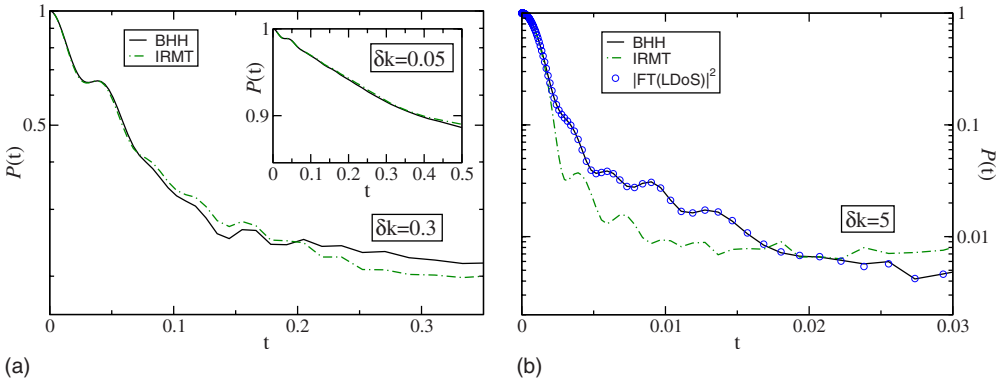

FIG. 18. (Color online) The survival probability $P(t)$ for the BHH and three different perturbation strengths (a) $\delta k=0.05<\delta k_{\mathrm{qm}}$ (inset), $\delta k_{\mathrm{qm}}<\delta k=0.3<\delta k_{\mathrm{prt}}$ (main figure) and (b) $\delta k=5>\delta k_{\mathrm{prt}}$. The solid black line represents the exact numerical result, while the dash-dotted green line is the LRT result (39) calculated using the IRMT model. The inset of panel (a) represents the FOPT regime, while the main figure corresponds to the extended perturbative regime. Here the break time is $t_{\mathrm{prt}}\sim 0.1$ (see Sec. VI B 2). In the nonperturbative regime (b), the LRT breaks down close to the calculated break time $t_{\mathrm{prt}}\sim 0.001$. In this panel we superimpose the Fourier transform of the LDOS as blue circles. The agreement with $\mathcal{P}(t)$ is excellent. Here, $N=230$, $\tilde{U}=280$, $\tilde{E}=0.26$, and $\lambda_0=0.053$.

the conclusion [18,28] that the LRT predictions are not applicable, while detailed QCC would possibly validate semiclassical considerations. We will examine this assumption more carefully in Sec. VI C.

What about the IRMT modeling? In the inset of Fig. 17(a) we report the numerical results for the spreading $\delta E(t)$ of the IRMT model. We observe that as soon as we enter the nonperturbative regime, the spreading $\delta E(t)$ shows a qualitatively different behavior than the dynamical BHH model. Namely, after an initial ballistic spreading (taking place for times $t<t_{\rm prt}$), we observe a premature crossover to a diffusive behavior $\delta E(t)=\sqrt{2D_E t}$. The following heuristic picture can explain the diffusive behavior of the IRMT modeling. At $t\sim t_{\rm prt}\ll\tau_{\rm cl}$, the evolving distribution becomes as wide as the bandwidth, and we have $\delta E_{\rm core}\sim\delta E\sim\Delta_b$ rather than $\delta E_{\rm core}\ll\delta E\ll\Delta_b$. Once the mechanism for ballisticlike spreading disappears, a stochasticlike behavior takes its place. This is similar to a random-walk process where the step size is of the order Δ_b, with transient time $t_{\rm prt}$.

The same deviations are observed for other observables as well. In Fig. 18(b) we report our results for the survival probability in the nonperturbative regime. We find that the IRMT modeling (which for short times gives the same results as LRT, not shown in the figure as they are indistinguishable from the IRMT results) breaks down after an initial Gaussian decay (41), which holds up to a break time $t_{\rm prt}\sim 0.001$. Instead, the behavior of $\mathcal{P}(t)$ can be obtained by a Fourier transform of the LDOS. Specifically, we have that

$$\begin{aligned}\mathcal{P}(t) &\equiv |\langle n(k_0)|e^{-i\hat{H}(k)t/\hbar}|n(k_0)\rangle|^2 \\ &= \left|\sum_m e^{-iE_m(k)t/\hbar}|\langle m(k)|n(k_0)\rangle|^2\right|^2 \\ &= \left|\int_{-\infty}^{\infty} P(E|m)e^{-iEt/\hbar}dE\right|^2, \end{aligned} \tag{43}$$

where $P(E|m)$ is given by Eq. (26). In Fig. 18(b) we superimpose the outcome of Eq. (43) (see blue circles) together with the survival probability evaluated by the numerical integration of the Schrödinger equation. An excellent agreement is evident.

C. Detailed versus restricted QCC

In the previous subsection we have assumed that the evolving wave packet is developing detailed QCC in the nonperturbative regime and for times $t>t_{\rm prt}=(\frac{\delta k_{\rm prt}}{\delta k})\tau_{\rm cl}$ (for earlier times FOPT—or equivalently IRMT considerations—apply).

In Fig. 19 we report four snapshots of the evolving quantum-mechanical profile (black lines). In the same figure we report the IRMT results (dash-dotted green lines) together with the classical calculations (blue lines with ○). As we have discussed above we distinguish two phases in the evolution: For $t<\tau_{\rm cl}$ the IRMT modeling (or equivalently the FOPT) is applicable, while for $t>\tau_{\rm cl}$ the evolving profile is described by its classical counterpart $P_{\rm cl}(t)$. During this second phase, the evolution predicted by the IRMT is diffusive, leading to a Gaussian shape for $P_t(n|m)$.

VII. CONCLUSIONS

In this paper we have studied the evolving energy distribution of a three-site ring-shaped Bose-Hubbard model in the chaotic regime. The evolution is triggered by a change δk in the tunneling rate k between neighboring lattice sites, which in the context of ultracold atoms in optical lattices is realized by a change in the intensity of the trapping laser field. The specific scenario that we have analyzed in detail is the so-called wave-packet dynamics in energy space corresponding to a constant driving pulse of finite duration t.

We followed a threefold approach to the problem which combines purely quantum-mechanical as well as semiclassical and random matrix theory considerations. This enabled us to identify both the strengths and limitations of each method.

We find the appearance of three dynamical δk regimes: the standard perturbative ($\delta k<\delta k_{\rm qm}\propto\tilde{U}/N^{3/2}$), the extended perturbative ($\delta k_{\rm qm}<\delta k<\delta k_{\rm prt}\propto\tilde{U}/N$), and the nonperturbative regime ($\delta>\delta k_{\rm prt}$). The first two regimes can be addressed using LRT or RMT calculations. In contrast, the last regime requires a combination of LRT and RMT calculations and semiclassical considerations. The former approach describes the evolving energy distribution for short times while the latter applies for longer times. Interestingly enough we have found that the variance $\delta E^2(t)$ of the evolving energy distribution shows a robust quantum-classical correspondence for all δk values, while other moments exhibit this QCC only in the nonperturbative regime identified with the classical limit. In this regime, even an improved RMT modeling fails to describe the long-time behavior of $\delta E(t)$, leading to a premature crossover from ballistic to diffusive behavior.

The motivation of the present study is driven both by theoretical and experimental considerations. On the fundamental level, we would like to understand the manifestation of quantum-classical correspondence in the context of quantum chaotic dynamics, where chaos enters not due to geometrical considerations ("chaotic" shape of the trap), but due to many-body interactions [83]. At the same time, our results are also of immediate relevance to various branches of physics. For example, in the framework of ultracold atoms loaded in optical traps one is interested in understanding measurements of the energy absorption rates induced by potential modulations [20–26]. Another application arises in molecular physics: As mentioned in Sec. II, the Bose-Hubbard Hamiltonian also models bond excitations in small molecules [57,84]. In this respect, the wave-packet dynamics investigated here describes the vibrational energy redistribution of an initial excitation [84].

As far as the experimental realization of our study is concerned, microtraps [8] are promising candidates for such time-dependent potentials [85], while optical lattices have already been successfully used in similar setups. Specifically, the studied dynamical scenario is readily implemented by changing the intensity of the laser field using a simplified version of the experiments of the Zurich group [20,21]. In contrast to the periodic modulation presented there, the optical lattice depth has to be altered in a steplike manner. Such

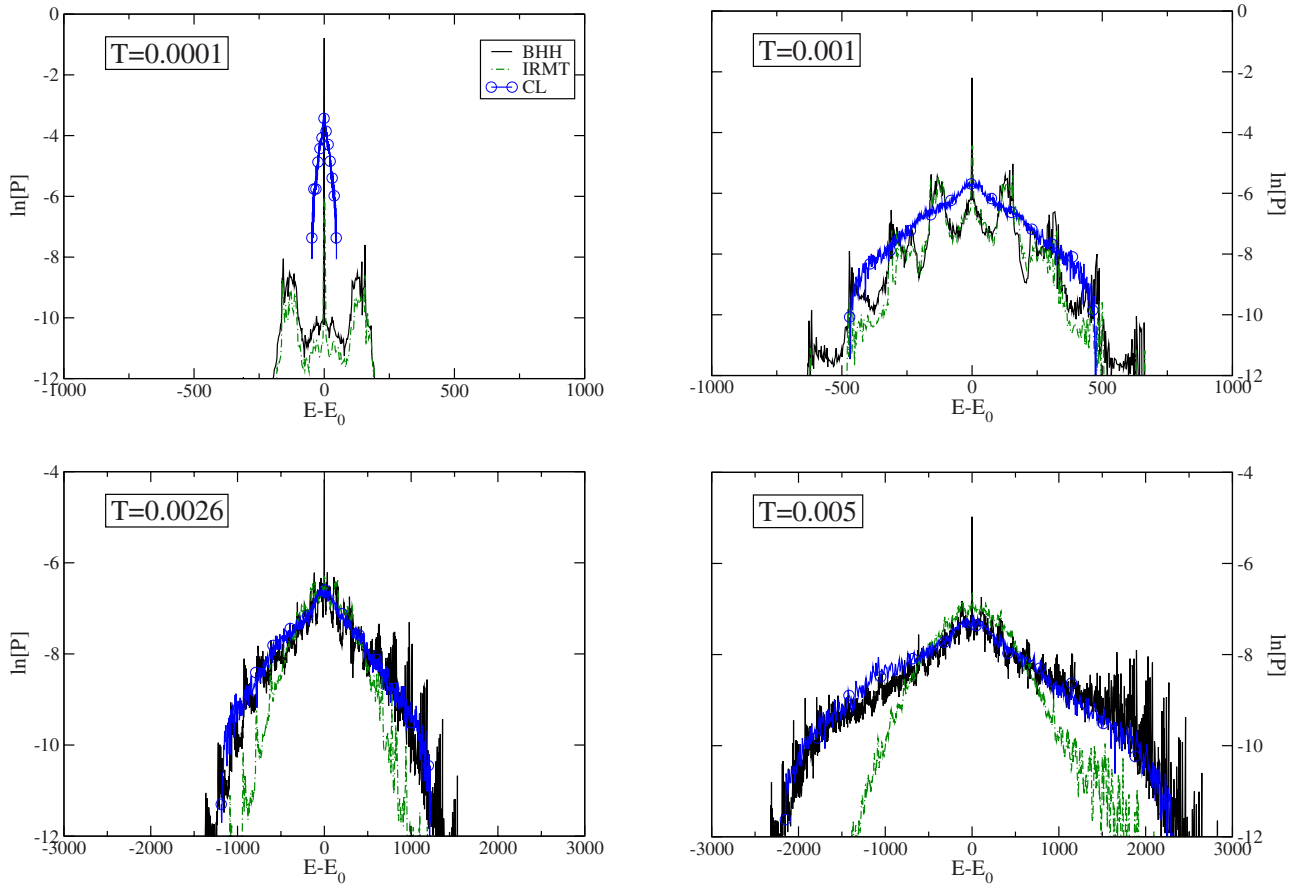

FIG. 19. (Color online) Snapshots of the evolving quantum profile $P_t(r)$ obtained from the BHH (black line) and the IRMT model (dash-dotted green line) as well as the classical profile $P_t^{\mathrm{cl}}(r)$ (blue line with ○) in the nonperturbative regime $\delta k=5>\delta k_{\mathrm{prt}}$ plotted against the energy difference $E-E_0$. After the quantal transition period $t\sim 0.002$ [see Fig. 17(b)], there is no scale separation between the core and the tail component and one observes overall detailed QCC. However, the initially excited component $|n_0\rangle$ decays slower in the quantum case. Here, $N=230$, $\tilde{U}=280$, $\tilde{E}=0.26$, and $\lambda_0=0.053$.

experiments have been successfully performed by Greiner *et al.* [86] where the intensity of the trapping laser field was suddenly raised. A rise time was achieved much faster than the tunneling time between neighboring sites, but slow enough so as not to excite higher vibrational modes of the wells.

Concerning the measurement of the energy distribution $P_t(E)$ and the associated absorption of energy due to the driving, various techniques may be applied. Using standard time-of-flight measurements, one can determine, for example, the release energy of the condensate and the momentum distribution of the atomic cloud, which we expect to provide the relevant information on the variance $\delta E^2(t)$ of the energy distribution. Another possibility is to probe the $P_t(E)$ via phase diffusion measurements [86]. Experimentally, the BEC can be prepared (almost) in one eigenstate. The driving pulse induces a broadening in the energy distribution, leading to (decaying) oscillations in the contrast $\langle b_i^\dagger b_{i+1}+b_i b_{i+1}^\dagger\rangle$ between neighboring sites. We expect that the functional form of the decay can be directly related to the core width Γ and thus be used to detect the three parametric δk regimes. While these measurements are in principle sensitive to decoherence due to residual interaction with the noncondensed atoms, we note here that for two-site systems coherence times of several hundred milliseconds were observed [88].

ACKNOWLEDGMENTS

The authors acknowledge fruitful discussions with Doron Cohen, Sergei Flach, George Kalosakas, and Markus Oberthaler. This research was supported by a grant from the United States–Israel Binational Science Foundation (BSF) and the DFG within the Forschergruppe 760.

[1] B. P. Anderson and M. A. Kasevich, Science **282**, 1686 (1998).
[2] D. Jaksch, C. Bruder, J. I. Cirac, C. W. Gardiner, and P. Zoller, Phys. Rev. Lett. **81**, 3108 (1998).
[3] F. S. Cataliotti, S. Burger, C. Fort, P. Maddaloni, F. Minardi, A. Trombettoni, A. Smerzi, and M. Inguscio, Science **293**, 843 (2001).
[4] C. Orzel, A. K. Tuchman, M. L. Fenselau, M. Yasuda, and M. A. Kasevich, Science **291**, 2386 (2001).
[5] R. Folman, P. Krüger, D. Cassettari, B. Hessmo, T. Maier, and J. Schmiedmayer, Phys. Rev. Lett. **84**, 4749 (2000).
[6] W. Hänsel, P. Hommelhoff, T. W. Hänsch, and J. Reichel, Nature (London) **413**, 498 (2001).
[7] H. Ott, J. Fortagh, G. Schlotterbeck, A. Grossmann, and C. Zimmermann, Phys. Rev. Lett. **87**, 230401 (2001).
[8] J. Reichel, Appl. Phys. B: Lasers Opt. **74**, 469 (2002).
[9] E. Andersson, T. Calarco, R. Folman, M. Andersson, B. Hessmo, and J. Schmiedmayer, Phys. Rev. Lett. **88**, 100401 (2002).
[10] T. Schumm, S. Hofferberth, L. M. Andersson, S. Wildermuth, S. Groth, I. Bar-Joseph, J. Schmiedmayer, and P. Krüger, Nat. Phys. **1**, 57 (2005).
[11] Y.-J. Wang, D. Z. Anderson, V. M. Bright, E. A. Cornell, Q. Diot, T. Kishimoto, M. Prentiss, R. A. Saravanan, S. R. Segal, and S. Wu, Phys. Rev. Lett. **94**, 090405 (2005).
[12] M.-O. Mewes, M. R. Andrews, D. M. Kurn, D. S. Durfee, C. G. Townsend, and W. Ketterle, Phys. Rev. Lett. **78**, 582 (1997).
[13] M. R. Andrews, C. G. Townsend, H.-J. Miesner, D. S. Durfee, D. M. Kurn, and W. Ketterle, Science **275**, 637 (1997).
[14] E. W. Hagley, L. Deng, M. Kozuma, J. Wen, K. Helmerson, S. L. Rolston, and W. D. Phillips, Science **283**, 1706 (1999).
[15] M. Greiner, O. Mandel, T. Esslinger, T. W. Hänsch, and I. Bloch, Nature (London) **415**, 39 (2002).
[16] U. Weiss, *Quantum Dissipative Systems* (World Scientific, Singapore, 1998).
[17] M. Wilkinson, *Parametric Random Matrices: Static and Dynamic Applications* (Kluwer Academic, New York, 1999), pp. 369–399.
[18] D. Cohen, Ann. Phys. (N.Y.) **283**, 175 (2000).
[19] M. Hiller, D. Cohen, T. Geisel, and T. Kottos, Ann. Phys. (N.Y.) **321**, 1025 (2006).
[20] T. Stoferle, H. Moritz, C. Schori, M. Kohl, and T. Esslinger, Phys. Rev. Lett. **92**, 130403 (2004).
[21] C. Schori, T. Stoferle, H. Moritz, M. Kohl, and T. Esslinger, Phys. Rev. Lett. **93**, 240402 (2004).
[22] C. Kollath, A. Iucci, T. Giamarchi, W. Hofstetter, and U. Schollwock, Phys. Rev. Lett. **97**, 050402 (2006).
[23] A. M. Rey, P. B. Blakie, G. Pupillo, C. J. Williams, and C. W. Clark, Phys. Rev. A **72**, 023407 (2005).
[24] A. Iucci, M. A. Cazalilla, A. F. Ho, and T. Giamarchi, Phys. Rev. A **73**, 041608(R) (2006).
[25] G. G. Batrouni, F. F. Assaad, R. T. Scalettar, and P. J. H. Denteneer, Phys. Rev. A **72**, 031601(R) (2005).
[26] E. Lundh, Phys. Rev. A **70**, 061602(R) (2004).
[27] D. Cohen, F. M. Izrailev, and T. Kottos, Phys. Rev. Lett. **84**, 2052 (2000).
[28] T. Kottos and D. Cohen, Phys. Rev. E **64**, 065202(R) (2001).
[29] M. Hiller, T. Kottos, and T. Geisel, Phys. Rev. A **73**, 061604(R) (2006).
[30] G. J. Milburn, J. Corney, E. M. Wright, and D. F. Walls, Phys. Rev. A **55**, 4318 (1997).
[31] O. Morsch and M. Oberthaler, Rev. Mod. Phys. **78**, 179 (2006).
[32] I. Bloch, J. Dalibard, and W. Zwerger, Rev. Mod. Phys. **80**, 885 (2008).
[33] R. Franzosi, V. Penna, and R. Zecchina, Int. J. Mod. Phys. B **14**, 943 (2000).
[34] J. C. Eilbeck, P. S. Lomdahl, and A. C. Scott, Physica D **16**, 318 (1985).
[35] G. P. Tsironis and V. M. Kenkre, Phys. Lett. A **127**, 209 (1988).
[36] L. Bernstein, J. C. Eilbeck, and A. C. Scott, Nonlinearity **3**, 293 (1990).
[37] G. Kalosakas, A. R. Bishop, and V. M. Kenkre, Phys. Rev. A **68**, 023602 (2003).
[38] M. Albiez, R. Gati, J. Folling, S. Hunsmann, M. Cristiani, and M. K. Oberthaler, Phys. Rev. Lett. **95**, 010402 (2005).
[39] A. Kasper, S. Schneider, C. vom Hagen, M. Bartenstein, B. Engeser, T. Schumm, I. Bar-Joseph, R. Folman, L. Feenstra, and J. Schmiedmayer, J. Opt. B: Quantum Semiclassical Opt. **5**, S143 (2003).
[40] L. Amico, A. Osterloh, and F. Cataliotti, Phys. Rev. Lett. **95**, 063201 (2005).
[41] G. Birkl and J. Fortagh, Laser Photonics Rev. **1**, 12 (2007).
[42] D. R. Scherer, C. N. Weiler, T. W. Neely, and B. P. Anderson, Phys. Rev. Lett. **98**, 110402 (2007).
[43] S. Levy, E. Lahoud, I. Shomroni, and J. Steinhauer, Nature (London) **449**, 579 (2007).
[44] J. C. Eilbeck, G. P. Tsironis, and S. K. Turitsyn, Phys. Scr. **52**, 386 (1995).
[45] R. Franzosi and V. Penna, Phys. Rev. A **65**, 013601 (2001).
[46] L. Casetti, M. Pettini, and E. G. D. Cohen, Phys. Rep. **337**, 237 (2000).
[47] S. De Filippo, M. Fusco Girard, and M. Salerno, Nonlinearity **2**, 477 (1989).
[48] L. Cruzeiro-Hansson, H. Feddersen, R. Flesch, P. L. Christiansen, M. Salerno, and A. C. Scott, Phys. Rev. B **42**, 522 (1990).
[49] K. Nemoto, C. A. Holmes, G. J. Milburn, and W. J. Munro, Phys. Rev. A **63**, 013604 (2000).
[50] J. D. Bodyfelt, M. Hiller, and T. Kottos, Europhys. Lett. **78**, 50003 (2007).
[51] R. A. Pinto and S. Flach, Phys. Rev. A **73**, 022717 (2006).
[52] A. R. Kolovsky and A. Buchleitner, Phys. Rev. E **68**, 056213 (2003).
[53] A. R. Kolovsky and A. Buchleitner, Europhys. Lett. **68**, 632 (2004).
[54] D. Cohen and T. Kottos, Phys. Rev. E **63**, 036203 (2001).
[55] M. Joyeux, S. Y. Grebenshchikov, J. Bredenbeck, R. Schinke, and S. C. Farantos, Adv. Chem. Phys. **130**, 267 (2005).
[56] F. Dalfovo, S. Giorgini, L. P. Pitaevskii, and S. Stringari, Rev. Mod. Phys. **71**, 463 (1999).
[57] A. C. Scott, P. S. Lomdahl, and J. C. Eilbeck, Chem. Phys. Lett. **113**, 29 (1985).
[58] E. Wright, J. C. Eilbeck, M. H. Hays, P. D. Miller, and A. C. Scott, Physica D **69**, 18 (1993).
[59] A. Chefles, J. Phys. A **29**, 4515 (1996).
[60] F. Haake, *Quantum Signatures of Chaos*, 2nd ed. (Springer-Verlag, Berlin, 2000).

[61] H.-J. Stöckmann, *Quantum Chaos: An Introduction* (Cambridge University Press, Cambridge, England, 1999).
[62] E. P. Wigner, Ann. Math. **62**, 548 (1955).
[63] E. P. Wigner, Ann. Math. **65**, 203 (1957).
[64] O. Bohigas, M. J. Giannoni, and C. Schmit, Phys. Rev. Lett. **52**, 1 (1984).
[65] M. V. Berry and M. Robnik, J. Phys. A **17**, 2413 (1984).
[66] T. A. Brody, Lett. Nuovo Cimento Soc. Ital. Fis. **7**, 482 (1973).
[67] T. A. Brody, J. Flores, J. B. Fench, P. A. Mello, A. Pandey, and S. S. M. Wong, Rev. Mod. Phys. **53**, 385 (1981).
[68] C. Petitjean, D. V. Bevilaqua, E. J. Heller, and P. Jacquod, Phys. Rev. Lett. **98**, 164101 (2007).
[69] M. Feingold and A. Peres, Phys. Rev. A **34**, 591 (1986).
[70] T. Prosen and M. Robnik, J. Phys. A **26**, L319 (1993).
[71] M. V. Berry, *Chaos and Quantum Systems* (Elsevier, Amsterdam, 1991).
[72] Y. Imry, *Introduction to Mesoscopic Physics* (Oxford University Press, New York, 1997).
[73] M. V. Berry, J. Phys. A **10**, 2083 (1977).
[74] T. Prosen, Ann. Phys. (N.Y.) **235**, 115 (1994).
[75] E. J. Austin and M. Wilkinson, Europhys. Lett. **20**, 589 (1992).
[76] M. Feingold, D. M. Leitner, and M. Wilkinson, Phys. Rev. Lett. **66**, 986 (1991).
[77] M. Feingold, A. Gioletta, F. M. Izrailev, and L. Molinari, Phys. Rev. Lett. **70**, 2936 (1993).
[78] Y. V. Fyodorov, O. A. Chubykalo, F. M. Izrailev, and G. Casati, Phys. Rev. Lett. **76**, 1603 (1996).
[79] F. M. Izrailev, T. Kottos, A. Politi, and G. P. Tsironis, Phys. Rev. E **55**, 4951 (1997).
[80] D. Cohen and E. J. Heller, Phys. Rev. Lett. **84**, 2841 (2000).
[81] J. A. Mendez-Bermudez, T. Kottos, and D. Cohen, Phys. Rev. E **72**, 027201 (2005).
[82] D. Cohen and T. Kottos, Phys. Rev. Lett. **85**, 4839 (2000).
[83] G. L. Salmond, C. A. Holmes, and G. J. Milburn, Phys. Rev. A **65**, 033623 (2002).
[84] K. Lehmann, G. Scoles, and B. Pate, Annu. Rev. Phys. Chem. **45**, 241 (1994).
[85] G.-B. Jo, Y. Shin, S. Will, T. A. Pasquini, M. Saba, W. Ketterle, D. E. Pritchard, M. Vengalattore, and M. Prentiss, Phys. Rev. Lett. **98**, 030407 (2007).
[86] M. Greiner, O. Mandel, T. W. Hänsch, and I. Bloch, Nature (London) **419**, 51 (2002).
[87] We thank N. Davidson (private communication) for pointing this out to us.
[88] M. Oberthaler (private communication).